Article

Measuring Local Viscosities near Plasma Membranes of Living Cells with Photonic Force Microscopy

Felix Jünger,[1] Felix Kohler,[1] Andreas Meinel,[1] Tim Meyer,[2] Roland Nitschke,[3] Birgit Erhard,[1] and Alexander Rohrbach[1,4,*]

[1]Laboratory for Bio- and Nano-Photonics, Department of Microsystems Engineering, University of Freiburg, Germany; [2]Macromolecular Modelling Group, Institute of Chemistry and Biochemistry, Freie Universität Berlin, Berlin, Germany; [3]Life Imaging Center (LIC) and Center for Biological Systems Analysis (ZBSA), University of Freiburg, Freiburg, Germany; and [4]BIOSS Centre for Biological Signalling Studies, University of Freiburg, Freiburg, Germany

ABSTRACT The molecular processes of particle binding and endocytosis are influenced by the locally changing mobility of the particle nearby the plasma membrane of a living cell. However, it is unclear how the particle's hydrodynamic drag and momentum vary locally and how they are mechanically transferred to the cell. We have measured the thermal fluctuations of a 1 μm-sized polystyrene sphere, which was placed in defined distances to plasma membranes of various cell types by using an optical trap and fast three-dimensional (3D) interferometric particle tracking. From the particle position fluctuations on a 30 μs timescale, we determined the distance-dependent change of the viscous drag in directions perpendicular and parallel to the cell membrane. Measurements on macrophages, adenocarcinoma cells, and epithelial cells revealed a significantly longer hydrodynamic coupling length of the particle to the membrane than those measured at giant unilamellar vesicles (GUVs) or a plane glass interface. In contrast to GUVs, there is also a strong increase in friction and in mean first passage time normal to the cell membrane. This hydrodynamic coupling transfers a different amount of momentum to the interior of living cells and might serve as an ultra-soft stimulus triggering further reactions.

INTRODUCTION

A biological cell can be considered as a minimal living system to respond to external disturbances. Among the many different kinds of stimuli that a cell is exposed to, mechanical contacts at the cell surface play a superordinate role (1,2), because cells are in constant mechanical interaction with their environment. The question of how a cell reacts to an approaching particle is of principal interest for various disciplines ranging from immunology (3,4) to drug delivery (5–7), and it is connected to the preceding question of how much time is given to a cell to react adequately to an approaching disturbance such as a bacterium, a virus, a vesicle, or inorganic particles delivered deliberately or unintentionally from outside.

The characteristic reaction time of a cell can be defined by a time period that starts with a stimulus of transmembrane receptors or of molecules in the pericellular/extracellular matrix (8), which can be measured by, e.g., small changes in the fluctuation amplitude of the approaching particle (9). The end of the reaction time can be defined by a measurable reorganization of membrane proteins or cytoskeleton proteins. This reaction can be further amplified by the duration and the amplitude of the stimulus, e.g., the ongoing approach of the particle. During the stimulus, the particle typically diffuses passively nearby the cell membrane on a timescale that is dominated by the viscosity of the extracellular fluid. Generally, the equilibrium association constant for two binding partners does not depend on the viscosity—provided reaction time is not limited. However, an increase of the viscosity η nearby the cell membrane is accompanied by a decrease of the collision rate $f_c \sim 1/\eta$ with the cell membrane and thus by decreased binding and reaction probability (10,11). The variation in the viscous drag $\gamma \sim \eta$ of the approaching particle regulates the transfer of hydrodynamic momentum to the cell and thereby the amplitude of a stimulus and eventually of the cellular response. In this study we investigate the distance-dependent behavior of the mobility $\mu = 1/\gamma$ near the membranes of living cells, which has been measured so far only in specific viscoelastic relaxation experiments (8).

The change of the viscosity experienced by a particle near a stiff plane interface, i.e., its hydrodynamic coupling to the wall, has been put on a solid theoretical basis by the 1963 work of Happel and Brenner (12), who were able to predict the increase of a particle's viscous drag parallel and perpendicular to the interface as a function of the separation distance. Theoretical studies by Lee (13,14) and Bickel (15,16) showed that the increase in static viscous drag at a fluid interface is very similar to that of a stiff interface in perpendicular direction, but is hardly visible parallel to the fluid interface. The theoretical work of Bickel (15) was extended to deformable membrane interfaces, considering different spatial and temporal frequencies at the deforming membrane (16).

Submitted November 4, 2014, and accepted for publication July 17, 2015.

*Correspondence: rohrbach@imtek.de

Editor: Jochen Guck.

0006-3495/15/09/0869/14

http://dx.doi.org/10.1016/j.bpj.2015.07.027

A variety of experimental efforts were undertaken to confirm the theoretical predictions of the space variant viscous drag or diffusion constants of microbeads at stiff planar interfaces and alterations thereof. This was either realized by video tracking of a diffusing particle (17), by evanescent wave scattering (18–20), by analyzing the bead fluctuations inside an optical trap (21,22) or attached to the cantilever of an atomic force microscopy (23), or by using fluorescence correlation spectroscopy of fluorescent beads (24). In this context, optical traps enabled the measurement of the Derjaguin-Landau-Verwey-Overbeek potential in combination with viscous relaxation experiments near the interface (25). Instead of mapping the position-dependent local diffusion normal to the interface, Pralle et al. (26) succeeded in mapping the changes in lateral diffusion inside plasma membranes revealing sphingolipid-cholesterol rafts.

More complex situations of hydrodynamic coupling lengths and temporal mode relaxation of several particles were investigated by either time multiplexed point traps (27–29), holographic optical traps (30,31), and optical line traps, enabling direct contact between the particles (32–34).

The most elegant way to measure local diffusion coefficients or viscous drags is to analyze the thermal position fluctuations of trapped particles. Whereas the analysis of fluctuation amplitudes provides information about the trapping potential and the local environment (35), the analysis of the position autocorrelation (AC) functions or the power spectral density (PSD) also enables the extraction of the viscous drag of the particle's motion (36). On very short timescales, this enables a three-dimensional (3D) viscosity mapping of small volume elements on the length scale of 10 to 30 nm (37).

Although the combination of optical traps and fast 3D position particle tracking, preferably by using back focal plane (BFP) interferometry, is quite established, no experiments have been performed to measure the distance-dependent change of the viscous drag near the plasma membrane of a living cell.

In this study, we investigate the change of the viscous drag close to the plasma membrane for three different types of mammalian cells and giant unilamellar vesicles (GUVs) (38). We analyze the 3D position fluctuations on a μs timescale to extract the viscous drag at the position of the diffusing particle, which is controlled by an optical trap. We show that the hydrodynamic coupling lengths normal to the cell membrane can be measured with good reproducibility, and demonstrate that this length can vary significantly for different cell types.

Theoretical background

Thermal position fluctuations

The bead's stochastic motion in the presence of linear external forces can be theoretically described by a Langevin equation (39). In our case, it can be well approximated by the following:

$$\overleftrightarrow{\gamma}(d) \times \dot{\mathbf{b}} + \left(\overleftrightarrow{\kappa}_{opt} - \overleftrightarrow{\kappa}_{cell}(d)\right) \times \mathbf{b} = \mathbf{F}_{th}(t), \quad (1)$$

where the position vector $\mathbf{b}(t)$ denotes the bead's displacement with respect to the trap center at a given time t, and d is the distance of the cell membrane to the center of the laser focus; see Fig. 1 *B*, The trap center is ~0.2 μm behind the laser focus because of the radiation pressure (9). As the condition for overdamped motion for a high-enough viscous drag γ (i.e., $\gamma^2 > 4m\kappa$) is fulfilled, the inertia term $m\cdot\ddot{\mathbf{b}}$ was neglected. The spherical particle is driven by an uncorrelated random thermal force $\mathbf{F}_{th}(t)$ with $\langle F_{th,j}(t) \times F_{th,j}(t+\tau)\rangle = 2\gamma_{jj} \times k_BT \times \delta(\tau)$, which accounts for the Brownian motion of the particle with thermal energy k_BT. Choosing the cell surface normal to one coordinate axis, $\overleftrightarrow{\gamma}$ is approximately a diagonal tensor with diagonal elements γ_{jj} being the viscous drag coefficients for each spatial dimension $j = x,y,z$. As all nondiagonal matrix elements $\gamma_{i\neq j}(d) = 0$ vanish, we can refer to the diagonal elements as $\gamma_j(d)$ instead of $\gamma_{jj}(d)$. In general, $\gamma_j(d)$ varies with the distance d to an obstacle, which in our case is the membrane of a living cell. To fit the data presented in the results section, we assume the diagonal drag coefficients γ_j to have the following form:

$$\gamma_j(d) \approx \gamma_0 \times \exp\left(-(d-R)/\Lambda_j\right) + \gamma_\infty, \quad (2)$$

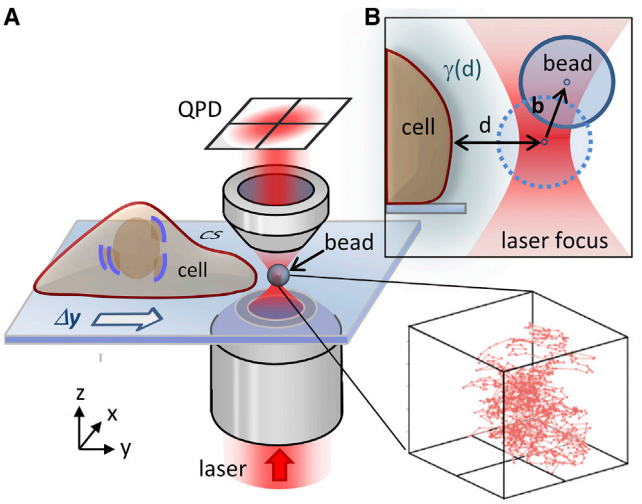

FIGURE 1 Sketch of the experimental setup. (*A*) A 1 μm polystyrene bead is fluctuating in the proximity of a living cell. An optical trap confines the motion of the particle to a small volume around the trap center with FWHM = 18 nm in x and y, and FWHM = 40 nm in z direction. The trap is moved toward the cell membrane with $\Delta y = 20$ nm steps by means of a 3D piezo stage. The bead's fluctuation data are recorded in three dimensions (lower right) with 2 MHz temporal resolution via two QPDs. For simplicity, only one QPD is drawn in this setup sketch. (*B*) The distance between the center of the optical trap and the cell membrane is denoted as d, whereas $\mathbf{b}$ symbolizes the bead's displacement from the trap center. The blue halo surrounding the cell membrane indicates the spatially varying viscous drag $\gamma(d)$. To see this figure in color, go online.

where Λ_j is the hydrodynamic coupling length in direction j and γ_∞ represents the viscous drag far away from the interface. $\gamma_0 = \gamma(d = R)$ describes the drag, when the bead with radius R is in contact with the cell membrane at $d = R$. $\overleftrightarrow{\kappa}_{opt}$ denotes the stiffness tensor of the optical trap and reflects the linearized restoring force $\mathbf{F} = \overleftrightarrow{\kappa}_{opt} \times \mathbf{b}$ for sufficiently small displacements, which is a valid assumption in all our experiments. Upon binding to a cell, an additional, a priori unknown stiffness parameter $\overleftrightarrow{\kappa}_{cell} \approx (\kappa_{cell,ij} \times \delta_{ij})$ contributes to the bead's motion. $\overleftrightarrow{\kappa}_{cell}$ can be approximated by a step-function, which is zero for distances $d > R$ to the membrane, such that the total force constant experienced by the particle in direction j is $\kappa_j(d) = \kappa_{cell,j}(d) + \kappa_{opt,j}$ such that $\kappa_j(d > R) \approx \kappa_{opt,j}$. Because both the optical force $\overleftrightarrow{\kappa}_{opt} \times \mathbf{b}$ and the friction force $\overleftrightarrow{\gamma}(d) \times \dot{\mathbf{b}}$ point in the opposite direction of $\mathbf{b}$ and $\dot{\mathbf{b}}$, respectively, they have the same sign. However, the force exerted by the cell, $-\overleftrightarrow{\kappa}_{cell} \times \mathbf{b}$, which only applies when $d < R$, tends to push the particle out of the trap, i.e., acts in the opposite direction and therefore has a negative sign.

A suitable and common method to determine the quantities κ and γ from the fluctuation data is correlation analysis (39). Assuming a linear force and friction acting on the particle in thermal equilibrium, the autocorrelation function for the particle's position is given by the following:

$$\begin{aligned} AC\big(b_j(t)\big) &= \big\langle b_j(t) \times b_j(t+\tau)\big\rangle \approx \big\langle b_j(0)^2\big\rangle \times e^{-\tau/\tau_{0j}} \\ &\approx \frac{k_B T}{\kappa_j(d)} \times \exp\big(-\tau \times \kappa_j(d)/\gamma_j(d)\big) \end{aligned} . \quad (3)$$

For time delays τ much shorter than the AC time $\tau_{0j} = \gamma_j/\kappa_j$, $AC(b_j(t)) = AC_j(\tau)$ is approximately linear, resulting in the following:

$$\begin{aligned} AC_j\big(\tau \ll \tau_{0j}\big) &\approx \frac{k_B T}{\kappa_j(d)}\big(1 - \tau \times \kappa_j(d)/\gamma_j(d)\big) \\ &= \frac{k_B T}{\kappa_j(d)} - \frac{k_B T}{\gamma_j(d)} \times \tau. \end{aligned} \quad (4)$$

The static part ($\tau = 0$) of the AC yields the stiffness parameter κ. The dynamical information extracted from the slope $k_B T/\gamma_j(d)$ of the AC for short time delays τ yields the friction coefficient γ.

Mean first passage time

The average time a particle needs to diffuse over a given distance is defined as the mean first passage time (MFPT). Often, diffusion of a particle over its own radius R is considered. In the absence of interfaces or for distances large enough that no disturbance of the diffusive motion occurs, i.e., $d\text{-}R >> \Lambda_j$, the MFPT simply reads $t_0 = (R^2/2k_B T) \times \gamma_\infty$, which can be derived from the particle's mean squared displacement (39). If hydrodynamic coupling to the interface has to be considered, i.e., for $d\text{-}R \approx \Lambda_j$, the spatial variation of the viscous drag has to be taken into account. For our exponential approach in Eq. 2, the following is the modified formula for the MFPT $t_j(d_1,d_2)$:

$$t_j(d_1, d_2) = \frac{R^2}{2k_B T} \times \frac{1}{d_2 - d_1} \int_{d_1}^{d_2} \gamma_\infty + \gamma_{0j} e^{-(d-R)/\Lambda_j} \mathrm{d}d, \quad (5)$$

where the multiplication with a constant factor γ_∞ has been replaced by an integral accounting for the distance-dependent change of $\gamma_j(d)$, normalized by the prefactor $(d_2\text{-}d_1)^{-1}$, and d_1 and d_2 are the boundaries confining the diffusion area in perpendicular direction.

Interferometric particle tracking and signal acquisition

The determination of the particle's displacement $\mathbf{b}(t)$ in our situation is not straightforward. The tracking scheme is based on intensities $I_{tot,2} = |\mathbf{E}_i + \mathbf{E}_p|^2$ generated by the interference of the electric field of the unscattered trapping light and the light scattered at the particle, $\mathbf{E}_i$ and $\mathbf{E}_p$. These intensities in the BFP are recorded by one or two quadrant photo diodes (QPDs); see Fig. 1. A QPD measures four voltage signals, each proportional to the interference intensity I_{tot}, which is integrated over the area of each quadrant. The voltage signals are then combined to result in three position signals $S_j(t)$ that are functions of the particle position $b_j(t)$. S_x is obtained from the difference of the two left and the two right quadrant signals, and S_y from the difference between the upper and lower two quadrant signals. The axial position signal S_z is provided by the sum of all four QPD signals and varies linearly with small axial displacements b_z of the particle. Therefore, the position signal recorded in the BFP of the detection objective lens (Fourier plane) with coordinates (k_x, k_y) can be described as $S_j(b_j) = \iint_{QPD} I_{tot,2}(k_x, k_y, b_j) H_j(k_x, k_y)\, dk_x dk_y$ (40). The vector function $\mathbf{H}$ is a filter selecting the three directions $j = x,y,z$ out of the interference pattern $I_{tot,2}$ through $\mathbf{H}(k_x, k_y) = step(k_0 NA_{\mathrm{det}} - |\mathbf{k}|) \times (2\, step(k_x) - 1,\ 2\, step(k_y) - 1,\ 1)$. $k_0 = 2\pi/\lambda$ is the vacuum wave number of the trapping light with wavelength $\lambda = 1.06\ \mu$m and $\mathrm{NA}_{\mathrm{det}}$ is the numerical aperture of the detection lens.

Within the small spatial displacements b_j occurring in all our experiments, the signals S_j are proportional to the actual displacements. The conversion factor is the detector sensitivity g_j and is given by $\mathrm{S(t)} = \overleftrightarrow{\mathrm{g}}\,\mathrm{(t)} \times \mathrm{b(t)}$. Before each experiment, i.e., in the absence of the cell, the undisturbed detector sensitivities $g_{\infty j}$ are determined by the Langevin calibration procedure (41).

If a particle diffuses nearby the cell, the incident trapping light can be scattered at the periphery of the cell as well, such that three beams with electric fields $\mathbf{E}_\mathrm{i}$, $\mathbf{E}_\mathrm{p}$, and $\mathbf{E}_\mathrm{c}$ (i = incident, p = particle, c = cell) can interfere. The three-beam interference generates an intensity pattern $I_{tot}(k_x, k_y)$ in the BFP of the detection objective lens (Fourier

plane) with coordinates (k_x, k_y) (40), which is imaged onto the QPD and can be described by (42) the following:

$$\begin{aligned} I_{tot,3}(\mathbf{b},d) &= \left|\mathbf{E}_i + \mathbf{E}_p(\mathbf{b}) + \mathbf{E}_c(d)\right|^2 \\ &= |\mathbf{E}_i|^2 + \left|\mathbf{E}_p\right|^2 + |\mathbf{E}_c|^2 \\ &\quad + 2|\mathbf{E}_i|\left|\mathbf{E}_p\right|\cos\left(\phi_i - \phi_p(\mathbf{b})\right) \\ &\quad + 2|\mathbf{E}_i||\mathbf{E}_c|\cos(\phi_i - \phi_c(-d)) \\ &\quad + 2\left|\mathbf{E}_p\right||\mathbf{E}_c|\cos\left(\phi_p(\mathbf{b}) - \phi_c(d)\right). \end{aligned} \tag{6}$$

The three-beam interference consists of six terms, with three additional intensities generated by the distance-dependent electric field $\mathbf{E}_c(d)$ scattered at the cell periphery. For large distances d, these terms vanish and the well-known two-beam interference formula is left over. Because the distance d is a positive number, we indicated the origin of the scattered phase $\phi_c(-d)$ by a negative argument, because the cell is placed left to the optical axis and the particle is right to the optical axis. Equation 6 can be summarized to the incoherent parts $I_i + I_p(\mathbf{b}) + I_c(d)$, two terms with sine functions both defined by the interference of the incident field and a scattered field, which are phase shifted by $\pi/2$, and, a cosine term defined by the interference between the two scattered fields, $\mathbf{E}_p$ and $\mathbf{E}_c$:

$$\begin{aligned} I_{tot,3}(k_x,k_y,\mathbf{b},d) \approx I_i + I_p(\mathbf{b}) + I_{ip}(\mathbf{b})\sin\left(\Delta\phi_{ip}(\mathbf{b})\right) \\ + I_c(d) - I_{ic}(d)\sin(\Delta\phi_{ic}(d)) \\ + I_{pc}(\mathbf{b},d)\cos\left(\Delta\phi_{pc}(\mathbf{b},d)\right). \end{aligned} \tag{7}$$

The second sine term does not change on timescales smaller than the measurement time, because it does not depend on the fluctuating particle position $\mathbf{b}(t)$. The cosine term, defined by both scattered fields, is small and can be neglected. According to Fig. 1 *B*, the cell is displaced in the one and the bead in the other direction relative to the center of the field's focus with phase ϕ_i. In this way, the two sine functions in Eq. 7 have different signs, because the phase difference $\Delta\phi_{ic}(d) = \phi_i - \phi_c(-d)$ is an odd function, i.e., $\Delta\phi_{ic}(d) = -\Delta\phi_{ic}(-d)$. Thereby, the distance-dependent term $I_{ic}(d)\sin(\Delta\phi_{ic}(d))$ flattens the total interference pattern across the QPD and reduces the mean value of the total signal $S_j(b_j,d)$ according to the following:

$$\begin{aligned} S_j(b_j,d) &\approx \int\!\!\int_{QPD} I_{tot,2}(b_j)H_j\,dk_x dk_y \\ &\quad + \int\!\!\int_{QPD} (I_c(d) - I_{ic}(d)\sin(\Delta\phi_{ic}(d)))H_j\,dk_x dk_y \\ &= S_{ip,j}(b_j) - S_{ic,j}(d). \end{aligned} \tag{8}$$

For small displacements, the position signal $S_{ip,j}(b_j(t)) \approx S_{0j} + g_{\infty j} \times b_j(t)$ is a linear function of displacements $b_j(t)$. According to Eq. 8, the distance-dependent signal $S_{ic,j}(d)$ generated by the cell reduces the measured signal $S_j(b_j,d)$ with decreasing distance d, but does not depend on the particle displacements b_j and thereby on the fluctuation width $\langle b_j(0)^2\rangle$. As shown by the green trajectory in Fig. 3 *A* , the vicinity of the cell will affect the mean signal offset, leading to an apparent particle displacement perpendicular to the cell surface, which is merely an optical effect. However, the amplitude of the position fluctuations $\langle b_j(0)^2\rangle$ is hardly affected.

Following Eq. 8, the AC of the particle's position signal is the sum of a time-varying and a temporally constant function, $AC(S(b(t),d)) = AC(S_{ip}(b(t)) - S_{ic}(d))$ and can be written as the sum of two AC functions: $AC(S(b(t),d)) = AC(S_{ip}(b(t))) + AC(S_{ic}(d)) - 2 \times CC(S_{ip}(b(t)), S_{ic}(d))$. The cross correlation between the conventional fluctuation signal and the DC signal from the cell is zero. The first AC function is the exponential of Eq. 3, the second is a wedge function characterized by the time-constant signal amplitude $S_{ic}(d)$.

$$\begin{aligned} AC\left(S_j(b_j,d)\right) &= g_j^2\frac{k_BT}{\kappa_j} \times \exp\left(-\frac{\tau\kappa_j}{\gamma_j(d)}\right) \\ &\quad + S_{ic,j}(d)^2\left(1 - \frac{\tau}{\tau_{mes}}\right) \\ &\overset{\tau<<\tau_{0j}}{\approx} g^2\left(\frac{k_BT}{\kappa_j} - \frac{k_BT}{\gamma_j(d)} \cdot \tau\right) + S_{ic,j}(d)^2. \end{aligned} \tag{9}$$

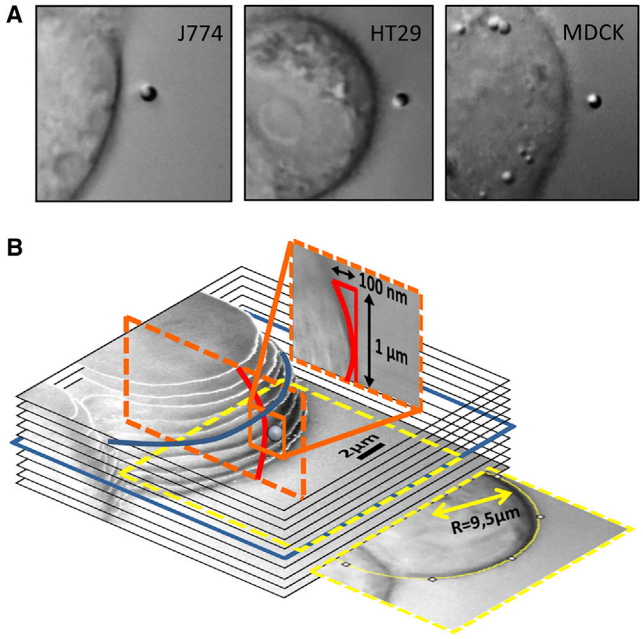

FIGURE 2 Three-dimensional configuration of the cell membrane interface. (*A*) DIC images of different cell types with a 1 μm diameter polystyrene bead. From left to right: J774 macrophage, HT29 adenocarcinoma cell, and MDCK epithelial cell. (*B*) Three-dimensional cell image of a HT29 cell, reconstructed from *x*-*y*-slices taken at different *z*-positions, which are $\Delta z = 1$ μm apart. The blue frame indicates the height above the cover slip at which the bead was placed. The additional slices illustrate the estimation of the cell's radii of curvature (*yellow frame*: *x*-*y*-plane, *orange and red lines*: *y*-*z*-plane). To see this figure in color, go online.

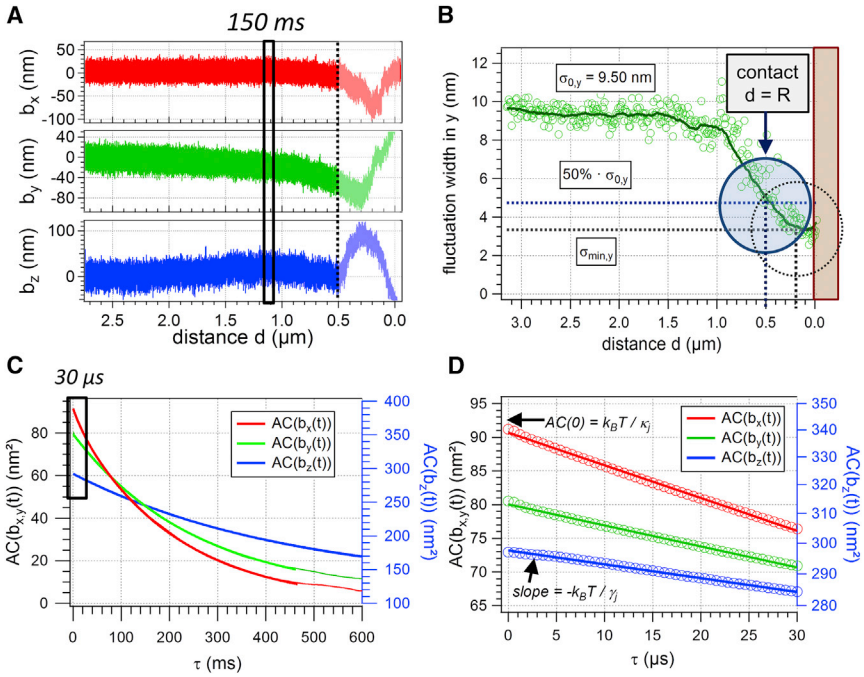

FIGURE 3 Analysis of a 1 μm bead's fluctuation data while approaching the membrane of a HT29 cell. (*A*) Distance-dependent position trajectories $b_x(d,t)$, $b_y(d,t)$, $b_z(d,t)$ calculated from the QPD data after calibration. *y* data correspond to scan direction. The regions $d \leq R$, in which the membrane is already in contact with the bead, are grayed out. The three-dimensional QPD data are divided into subsequent parts with duration $\tau_{mes} = 150$ ms as indicated by the black box; each spatial dimension is analyzed separately. (*B*) Upon contact to the membrane, i.e., $d = R$, the histogram width $\sigma_y(d)$ of the bead's fluctuations perpendicular to the cell membrane decreases (*circles*: data points, *solid line*: running average over 10 data points). The values at 50% of σ_0 and σ_{min} are used to determine the likely and the latest membrane contact point. The shaded region right of the vertical $d = 0$ line represents the cell. (*C*) The parts of the trajectory that correspond to one specific cell-focus distance *d* are analyzed by means of AC functions. (*D*) The AC is approximately linear on a $\tau \leq 30$ μs timescale, which is used to obtain $\kappa_j(d)$ and $\gamma_j(d)$. To see this figure in color, go online.

However, on short timescales $\tau << \tau_{0j}$, $\tau << \tau_{mes}$, the additional signal $S_{ic}(d)$ generated by the cell does not affect the slope $k_BT/\gamma_j(d)$ of the AC function and thereby the viscosity $\gamma_j(d)$. Here, the measurement time at each trap position, $\tau_{mes} = 150$ ms, equals ~100 times the AC time τ_{0j}.

MATERIALS AND METHODS

Optical microscope

An inverted microscope (Axio Observer, Carl Zeiss, Jena, Germany) equipped with a high NA water immersion objective lens (C-Apochromat 63×/ 1.20W Corr M27, Carl Zeiss) was used for differential interference contrast (DIC) and bright-field microscopy. The DIC images were acquired by a 12-bit monochrome charge-coupled device camera (AxioCam MRm, Carl Zeiss).

Photonic force microscope

In brief, the photonic force microscope consists of an optical trapping unit and an interferometric tracking unit. The optical trap is formed by a 2 W Nd:$GdVO_4$ solid-state laser (Smart Laser Systems, Berlin, Germany) operating at 1064 nm in cw mode, which is focused onto the sample via the objective lens. An acousto-optical modulator (AA.MT.110/A1-ir, AA Opto-Electronique, Orsay, France) allowed for the control of the laser power in the focus. The laser power is stabilized by a noise eater (miniNE 2.1, TEM Messtechnik, Hanover, Germany), which analyzes the laser intensity fluctuations by a reference photo diode (G8370-81, InGaAs photo diode, Hamamatsu, Japan) and controls the transmission of the acousto-optic modulator via an external regulation circuit. A simplified sketch of the experimental setup is shown in Fig. 1.

Tracking unit

A second high NA objective lens (W Plan-Apochromat 63×/ $NA_{det} = 1.0$, Carl Zeiss) is used to collect the unscattered laser light and the light scattered at the bead and the cell periphery, respectively. The resulting interference patterns in the BFP are imaged onto two QPDs (InGaAs PIN photodiodes, G6849 series, Hamamatsu). The beam is split up by 50% beam splitter cubes after passing the detection objective and is imaged onto the QPDs with different magnifications, accounting for the different detection sensitivities for axial and lateral signals, respectively (43–45). The use of InGaAs photodiodes enables high-speed tracking with good quantum efficiency at 1064 nm. Incoming voltage signals are amplified by two miniSupply QUAD pre-amplifiers (TEM Messtechnik) and digitalized via two analog-digital converter cards (NiDAQ PCI-6110 and PCIe-6259, National Instruments, Austin, TX).

Cell preparation

For our cell experiments, we used J774 mouse macrophages (American Type Culture Collection ATCC, Manassas, VA) as an example for cells that exhibit phagocytic activity as well as HT29 human colorectal adenocarcinoma cells and Madin-Darby canine kidney (MDCK) epithelial cells, the latter two showing no phagocytic activity. The cells, shown in Fig. 2, were cultured at 37°C in an atmosphere containing 5% CO_2. During growth and experiments, the cells were suspended in cell medium (Dulbecco's Modified Eagle Medium (DMEM GlutaMAX, Invitrogen Life Technologies, Carlsbad, CA) with 10% fetal bovine serum added). Before each experiment, the cells were detached from the bottom of the cell culture flask and transferred onto an uncoated microscope cover glass that has been sterilized before in an autoclave. No substrate coating of the microscope glass slides is necessary, as all cell types used in this study are adherent cells. The measurement chamber containing the cover glass and freshly added cell medium was kept at 37°C during all the experiments.

Sample chamber with heating unit

The temperature of the cell medium inside the sample chamber can be controlled by a surrounding heating element (TC-CSC, Bioscience Tools, San Diego, CA), which has an integrated temperature sensor and is regulated via a proportional-integral-derivative controller (TC-2-100, Bioscience Tools). The heating unit is switched on ~1 h before the experiments

to allow the system to equilibrate, thus reducing thermal drifts during measurement. The sample chamber is connected to 3D piezo stage (NanoView LP200, Mad City Labs, Madison, WI) that provides a 200 μm range of motion with a step response of 20 ms for each dimension and with a positioning accuracy smaller than 1 nm. Moving the sample chamber relative to the static optical trap thus enables an accurate distance control.

RESULTS

Geometrical arrangement

The geometry of the interfaces is an important factor in all experiments. We have approximated the cell to be planar over the cross section of the bead. To back up this assumption, the cell's radii of curvature were measured with the public domain software ImageJ (http://rsbweb.nih.gov/ij/) and compared with the bead's radius. For the sample cell shown in Fig. 2 *B*, the radius of curvature in the *x*-*y*-plane of ~9.5 μm is 19 times larger than the bead radius $R_{bead} =$ 0.5 μm, so that $R_{cell} >> R_{bead}$ is a valid assumption. All other cells used were of comparable size. In fact, the curvature of the cell has only a minor effect of <2.5% on the measured viscous drag $\gamma(d)$ that can be estimated by some geometrical considerations (see Figs. S1 and S2 in the Supporting Material).

The *z*-distance of the bead to the cover slip was chosen high enough, i.e., at least five times the bead diameter, where the hydrodynamic effects are low, such that no interaction between bead and cover slip could deteriorate our measurements. The direction of light propagation is always denoted as *z*, whereas the in-plane coordinates *x* and *y* are chosen such that *x* always denotes the direction parallel to the interface and *y* corresponds to the scan direction, i.e., perpendicular to the interface; see also Fig. 1. In the analysis of the hydrodynamic decay lengths and MFPTs, we limit ourselves to *x* and *y* data, to which we refer as $\parallel$ and $\perp$, respectively.

Measuring the position signals

QPD signals were recorded with a sampling rate of 2 MHz, from which the bead's position trajectories $b_x(t)$, $b_y(t)$, $b_z(t)$ were calculated as shown above; see Fig. 3 *A*. During data acquisition, the piezo stage holding the cell sample was moved in *y* direction with 20 nm steps, hereby subsequently reducing the distance *d* between the center of the laser focus and the cell membrane. At each step, 300,000 data points were recorded, corresponding to a measurement time $\tau_{mes} =$ 150 ms per position. This equals ~100 times the AC time, which has been shown to be beneficial for the reliability of the AC analysis presented in Fig. 3, *C* and *D*. The complete trajectories $b_x(t)$, $b_y(t)$, $b_z(t)$ were cut into single segments corresponding to one fixed piezo position and analyzed separately. Although the full range of data points up to $d = 0$ is shown in Fig. 3 *A*, only distances $d \geq R$ are considered for data evaluation. For $d < R$, bead and membrane are already in close contact, so that the fluctuation width of the bead is narrowed and causing the bead to be shifted out of the laser focus, which can be seen as a strong displacement of the trajectories in all spatial dimensions. A control experiment of an empty trap approaching a cell membrane is presented and discussed in the Supporting Material; see Fig. S3.

Estimating the contact between bead and membrane

From the fluctuation data in scan direction, i.e., *y* data, position histograms were determined and the distance-dependent standard deviation of the bead trace $\sigma_y(d)$ was analyzed; see Fig. 3 *B*. A decay of $\sigma_y(d = R) = 50\% \times \sigma_0$ to half of its bulk value reveals the position $d = R$, where the bead and a stiff interface are in mechanical contact (46). The rationale behind this choice is further explained in the Supporting Material, alongside data from Brownian dynamics simulations that back up this criterion; see Figs. S4–S7.

However, if the bead comes into contact with a soft interface, such as the pericellular matrix (PCM), the bead's fluctuation width can decay to $\sigma_0/2$ before contact with the cell membrane, which might be only reached at a minimal width of about $\sigma_y(d = R) \approx \sigma_0/3 = \sigma_{min}$. At this point, stiff membrane contact is very probable, as the bead starts to get pushed out of the optical trap by the cell and the QPD signals merely arise from laser light scattered at the cell. The true membrane contact point is likely located between these two estimates. More precise values for the membrane contact point cannot be specified, because a certain influence of the PCM on the measured signals remains. Analysis of all $\sigma(d)$ curves from each cell experiment reveals that the latest membrane contact point at σ_{min} is in average 0.22 μm $\pm$ 0.09 μm behind the 50% σ_0 estimate and differs slightly between different cell types (J774: 0.27 $\pm$ 0.09 μm, MDCK: 0.19 $\pm$ 0.07 μm, HT29: 0.21 $\pm$ 0.11 μm).

Force constants and distance-dependent viscosities

We can assume the system to be in thermal equilibrium as long as no contact between bead and membrane is established. Then, the fluctuation data can be analyzed by means of correlation analysis to obtain information about the force constants κ_j and the friction coefficients γ_j; see Eq. 4. Fig. 4 *A* shows the stiffness $\kappa(d)$ for varying distance *d* between the center of the laser focus and the cell membrane. All its components κ_j ($j = x,y,z$) remain constant until mechanical contact between the bead and the cell membrane is established, as indicated by additional line fits. The values obtained from these fits ($\kappa_x = 50.8$ pN/μm, $\kappa_y = 47.6$ pN/μm, $\kappa_z = 13.4$ pN/μm) agree well with the trap stiffnesses obtained from a Langevin-calibration before the experiment (not shown).

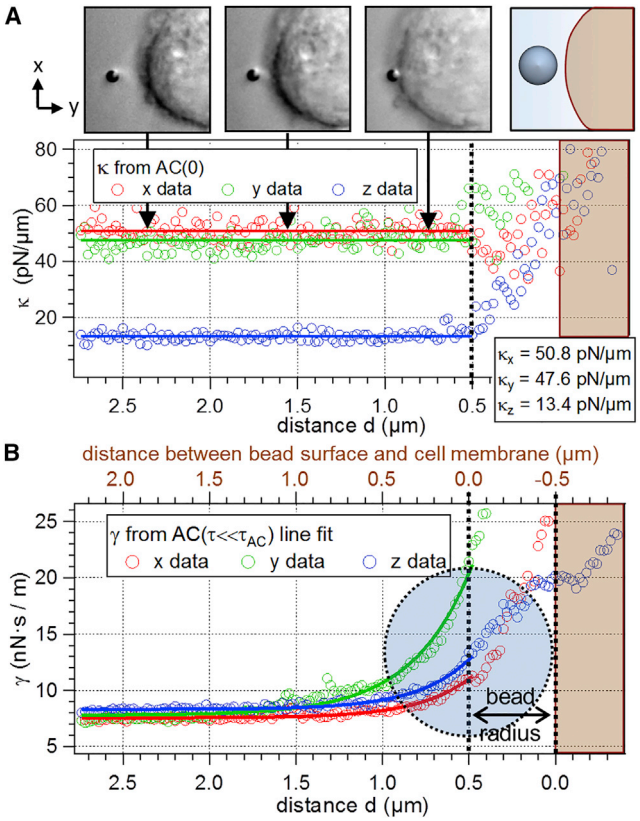

FIGURE 4 The bead's distance d to the cell membrane of a HT29 cell is subsequently decreased, as illustrated in the DIC images and the schematic sketch. Contact between the bead surface and the cell membrane is marked by a vertical dotted black line at $d = 0.5$ μm. (*A*) The stiffness parameter $\kappa_j(d)$ and (*B*) the viscous drag $\gamma_j(d)$ are plotted as a function of d. Solid lines in (*B*) indicate exponential fits to the data points. The positions of bead and cell (according to the 50% σ_0 criterion) are indicated by the filled circle and the shaded region right of $d = 0$. To see this figure in color, go online.

At the same time, the friction coefficients $\gamma_j(d)$ increase as the bead approaches the cell membrane, starting ~1 μm before contact. The increase of the friction component perpendicular to the cell membrane, i.e., $\gamma_y(d)$ displayed in green, is significantly higher than $\gamma_x(d)$ and $\gamma_z(d)$ in parallel direction (*red and blue circles*). This phenomenon has also been observed qualitatively in experiments of a spherical bead approaching a stiff wall (22).

Influence of filopodial binding on the fluctuation data

Macrophages are components of the mammalian immune system and possess small cell protrusions called filopodia, which can act as tentacles to pull bound objects toward the cell to initiate a process called phagocytosis (47,48). The measurements performed with macrophages require special attention because of possible binding events to cellular protrusions such as filopodia. Binding to such protrusions would make it impossible to extract information about pure hydrodynamic coupling out of the fluctuation data. During all experiments with cells, care was taken to investigate only parts of the membrane where no protrusions could be observed in the DIC images. However, binding to tiny filopodia that are invisible in the microscope can still have an influence on the measurement data and must be disregarded, if any changes in the fluctuation width become visible in the particle tracking data before cell contact. Upon binding to the membrane, the particle fluctuation width reduces strongly and considerable forces would be required to detach the particle from the cell (49).

Fig. 5 illustrates how filopodial binding can be identified in the fluctuation data. First, the bead's positions trajectories change slowly in their mean position values. Further analysis of the fluctuation behavior reveals that both $\kappa_j(t)$ and $\gamma_j(t)$ increase abruptly upon binding of a filopodium, while at the same time the fluctuation volume is restricted by the filopodium, resulting in a narrowed fluctuation width. The increase in $\kappa_j(t)$ and $\gamma_j(t)$ is most pronounced in the direction of filopodial retraction. As shown in Fig. 5, $\kappa_x(t)$ and $\kappa_y(t)$ increase rapidly to ~250% of their original values. $\gamma_x(t)$ and $\gamma_y(t)$ increase even by a factor of 10. Note that this behavior is fundamentally different to the smooth increase shown in Fig. 4. In this way possible filopodial binding can be identified with the help of the fluctuation data. For all results shown in the following chapters, we could verify that no filopodial binding occurred.

The pericellular matrix of living cells

A large variety of eukaryotic cells including those examined in this study are known to have a structure that is covalently linked to the outer side of the plasma membrane, the so-called

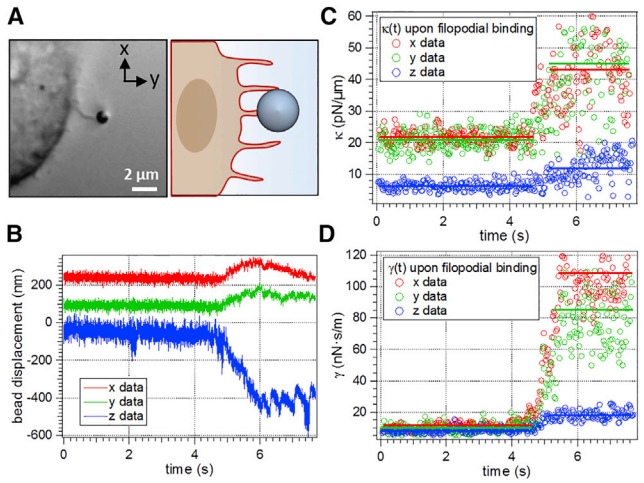

FIGURE 5 (*A*) DIC image and illustration of binding events to filopodia of a J774 macrophage. (*B*) Binding events can be seen in a relatively slow temporal change of the fluctuation data. Here, the binding process takes place at approximately $t = 4.8$ s. (*C* and *D*) An abrupt increase of both $\kappa_j(t)$ and $\gamma_j(t)$ in all three dimensions $j = x,y,z$ of up to one order of magnitude is observed upon binding, as filopodial retraction takes place in three dimensions. To see this figure in color, go online.

glycocalyx or PCM (8,49–51). It consists in particular of proteoglycans and associated polymer chains and is involved in plenty of cellular functions from cell adhesion and migration to receptor functions and immune response, only to mention a few. The thickness of the glycocalyx can exceed a few micrometers. As the PCM is invisible in brightfield or DIC microscopy, its occurrence is difficult to observe. However, its possible influence on the bead's fluctuation upon cell approach must not be ignored. A discussion of possible effects will be provided later in the manuscript.

Change of the local hydrodynamics close to a living cell

The distance-dependent viscous drag close to an interface is displayed in Figs. 4 and 6. The exponential function given in Eq. 2 was fitted to the data points $\gamma_j(t)$. The good fit results show that our exponential model is a suitable approach, which has the great advantage, that the hydrodynamic coupling of particles to the interface can be described by just two values for each direction, γ_{0j} and Λ_j. The hydrodynamic decay length Λ_j is a measure for the distance, on which hydrodynamic coupling between the particle and cell increases the friction. In the limit $d \rightarrow \infty$, i.e., far away from the cell, we measured a viscous drag $\gamma_\infty = 8.0 \times 10^{-9}$ Ns/m, which is the viscosity of the cell medium at $T = 37°C$ (52). $\gamma_\infty + \gamma_{0j}$ is the maximum viscous drag that occurs when cell membrane and bead surface are in close contact.

Fig. 6 summarizes the fit results to the measured $\gamma_j(d)$ curves for different cell samples using the contact point estimate at σ_0. In total, we investigated $N = 16$ J774 macrophages, $N = 15$ MDCK cells, $N = 24$ HT29 cells, and $N = 11$ GUVs. $\gamma_\perp(d)$ reveals comparable slopes for all cell types, but does not increase as steeply as for the case of a stiff wall at small distances, i.e., $0.5\ \mu m < d < 0.65\ \mu m$. Although $\Lambda_\perp$ is significantly higher than $\Lambda_\parallel$ for all living cells, this is not the case for a GUV or a glass interface. The hydrodynamic decay lengths for perpendicular motion are approximately the same for the J774 ($\Lambda_\perp = 0.49\ \mu m$) and the HT29 cells ($\Lambda_\perp = 0.45\ \mu m$), whereas the decay length for the MDCK cells is ~30% longer ($\Lambda_\perp = 0.65\ \mu m$). A similar result can be observed for the parallel decay lengths, which are generally ~1.5 to 1.8 times smaller: J774: $\Lambda_\parallel = 0.27\ \mu m$, HT29: $\Lambda_\parallel = 0.28\ \mu m$, MDCK: $\Lambda_\parallel = 0.34\ \mu m$. The viscous drag increases with decreasing distance d between focus and interface and, within our measurement accuracy, reaches a finite value $\gamma_j(d = R) = \gamma_{0j} + \gamma_\infty$; see Eq. 2 with $j = \perp, \parallel$. The obtained γ_0 values are displayed in Fig. 6 *C* as a multiple of $\gamma_\infty = 8.0 \times 10^{-9}$ Ns/m. In the case of diffusion parallel to the interface, the viscous drag $\gamma_{0\parallel}$ is effectively the same for all cell types investigated and increases to roughly 280% of the bulk value. The perpendicular friction factor $\gamma_{0\perp}$ is generally higher than $\gamma_{0\parallel}$ and the values for different cell types differ by up to

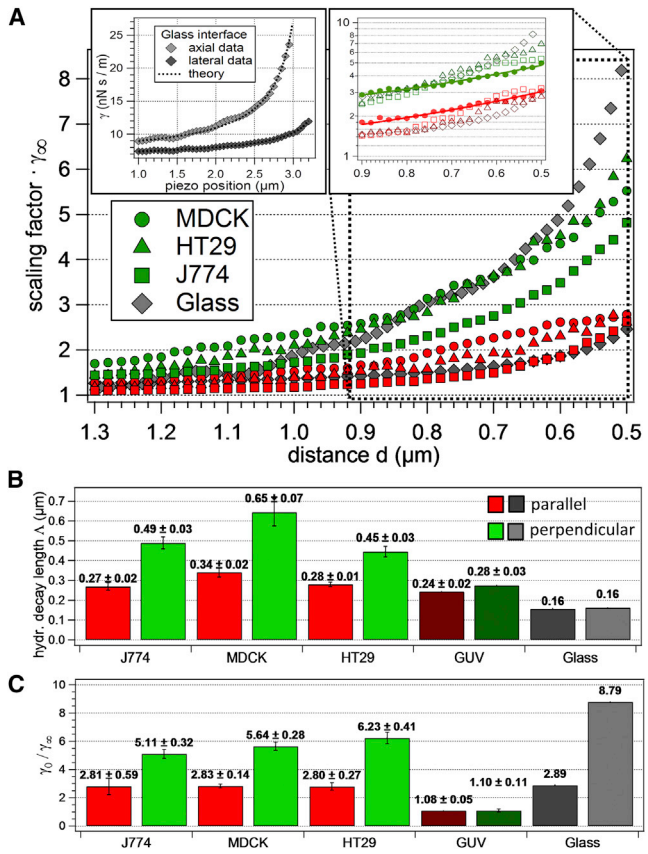

FIGURE 6 Hydrodynamic coupling of a 1 μm bead close to different interfaces. (*A*) Comparison of $\gamma_\perp(d)$ in green and $\gamma_\parallel(d)$ in red for all cell types and a stiff glass interface, shown in gray diamonds and in the upper left inset together with fits. Data points for all available measurements belonging to the respective cell type were averaged to get the resulting curves. The linear behavior in semi-logarithmic representation (*right inset*) confirms the nearly exponential decay, highlighted for the case of the MDCK cells. (*B*) Bar diagram of hydrodynamic decay lengths $\Lambda_\perp$ and $\Lambda_\parallel$ for all investigated cell types, the GUVs and the glass interface. (*C*) Summary of the measured values $\gamma_{0\perp}$ and $\gamma_{0\parallel}$ in units of $\gamma_\infty = 8.0 \times 10^{-9}$ Ns/m. Numbers in (*B*) and (*C*) are mean values ± standard deviation. GUV data in (*B*) and (*C*) are displayed in darker colors and glass data in gray, where dark gray represents parallel and light gray perpendicular data. To see this figure in color, go online.

20% from one another (HT29: $\gamma_{0\perp} = 6{,}23 \times \gamma_\infty$, MDCK: $\gamma_{0\perp} = 5{,}64 \times \gamma_\infty$, J774: $\gamma_{0\perp} = 5{,}11 \times \gamma_\infty$).

Using the σ_{min} criterion for the contact point, the measured decay lengths Λ_j are slightly decreased (by maximally 12%) and the maximum friction coefficients γ_{0j} are increased by a factor of 1.39 to 2.31, depending on the cell type. A detailed comparison of all the results is given in the Supporting Material; see Tables S1–S3, together with a revision of Figs. 6, *B* and *C*, and 7 accounting for the uncertainty of the membrane position (see Figs. S8–S10).

The change in $\gamma(d)$ of a bead approaching a plane stiff interface as a function of distance is well understood and can be theoretically calculated according to Happel's and Brenner's law (12). The corresponding measurement data is shown in the left inset of Fig. 6 *A*. The uncoated glass

cover slip of the measurement chamber was used to study the viscosity close to a stiff and planar interface, which leads to a different experimental geometry, as explained in the following and in the Supporting Material; see Figs. S11 and S12. In contrast to the cell experiments, where the surface was approached in y direction, the glass cover slip was approached in $-z$ direction, i.e., in (reverse) propagation direction of the laser light with $\Delta z = 20$ nm steps as in the cell experiments. To compensate for the weaker trap stiffness in z direction compared with x and y, the laser power was increased by 50% compared with the cell experiments.

The good agreement between our experimental data and the decay predicted by Happel and Brenner for the glass interface proves the validity of our measurement procedure. Applying our exponential decay model to the glass interface data yields decay lengths of $\Lambda_\perp = 0.162$ μm and $\Lambda_\parallel = 0.157$ μm. These values do not exhibit a difference in both directions, but are significantly lower than those for living cells, i.e., about a factor of 3.5 for perpendicular and 1.9 for parallel motion. One should note that fitting the Happel and Brenner functions

$$\gamma_\parallel = \gamma_\infty \left(1\text{-}9/16(R/d) + 1/8(R/d)^3\text{-}45/256(R/d)^4 \text{-}1/16(R/d)^5\right)^{-1} \quad (10)$$

$$\gamma_\perp = \gamma_\infty \left(6(d\text{-}R)^2 + 9 \times (d\text{-}R) \times R + 2R^2\right) / \left(6(d\text{-}R)^2 + 2 \times (d\text{-}R) \times R\right) \quad (11)$$

to the $\gamma(d)$ curves belonging to cell membranes or GUVs fails and that our exponential model shows more accurate fit results (not shown).

Measurements on GUVs as artificial cells

We have used GUVs as the simplest biomimetic model system for mammalian cells. As described in further detail by Meinel et al. (38), the GUVs were ~20 μm in diameter and were prepared from egg phosphatidylcholine (Egg PC, Sigma-Aldrich, St. Louis, MO), utilizing the method of electroformation. Different to the cells used, the GUVs are characterized by a lipid bilayer that separates two approximately identical fluids. Measurements on GUVs were performed with 1 μm–sized polystyrene beads and the same experimental parameters as described above, but with reduced laser power, resulting in slightly larger fluctuation volumes of the bead. The GUV was trapped in a sandwich configuration consisting of two uncoated glass cover slips separated by a 75 μm–thick spacer ring. Glass beads ($2R = 20$ μm) were attached to the downside of the upper cover slip to ensure the immobilization of the GUV, which has moved to the upper cover slip upon laser irradiation because of the scattering force.

Remarkably, and in contrast to the results for living cells, no significant difference in perpendicular and parallel hydrodynamic decay lengths ($\Lambda_\perp = 0.28$ μm, $\Lambda_\parallel = 0.24$ μm) could be observed; see Fig. 6 *B*. Both decay lengths are very similar to those $\Lambda_\parallel$ measured nearby living cells. The maximal friction close to the GUV membrane in perpendicular and in parallel direction are about the same ($\gamma_{0\perp} = 1.10 \times \gamma_\infty$ and $\gamma_{0\parallel} = 1.08 \times \gamma_\infty$), again significantly different compared with the results of living cells. The fluctuation data from the GUV experiments and the extraction of $\kappa_j(d)$ and $\gamma_j(d)$ similar to the procedure shown in Fig. 4 is presented in the Supporting Material; see Fig. S13, together with Fig. S14 displaying the bead's trajectory upon approaching the GUV membrane.

Mean first passage times

By means of Eq. 5, we analyzed the time a 1 μm bead needs to diffuse toward an interface from the distance $d_1 = 3R$ toward $d_2 = 2R$ with $t_0 = (R^2/2k_BT) \times \gamma_\infty = 0.234$s for $d\text{-}R >> \Lambda_j$ using the $\sigma_0/2$ criterion for the contact point. As Fig. 7 shows, the increase in viscous drag nearby an interface causes the MFPTs to rise significantly. For living cells, an anisotropy of the MFPT is apparent. The diffusion perpendicular to the membrane is slowed down by a factor of up to 1.64 in the case of MDCK cells (J774: $t_\perp(3R,2R) = 1.45 \times t_0$, HT29: $t_\perp(3R,2R) = 1.39 \times t_0$). In contrast, however, the MFPT for diffusion parallel to the interface is not affected severely, with a maximum increase of $t_\parallel(3R,2R) = 1.18 \times t_0$ for the case of MDCK cells. The significantly increased $t_\perp$ is unique to living cells and is not that pronounced at the GUV membrane with $t_\perp(3R,2R) = 1.08 \times t_0$ and $t_\parallel(3R,2R) = 1.06 \times t_0$. As the uncertainty in the determination of the true membrane contact point affects both Λ_j and γ_{0j}, the t_j are also influenced. Using the σ_{min} contact estimate results in an overall increase of t_j, which is again most pronounced in perpendicular direction. The results

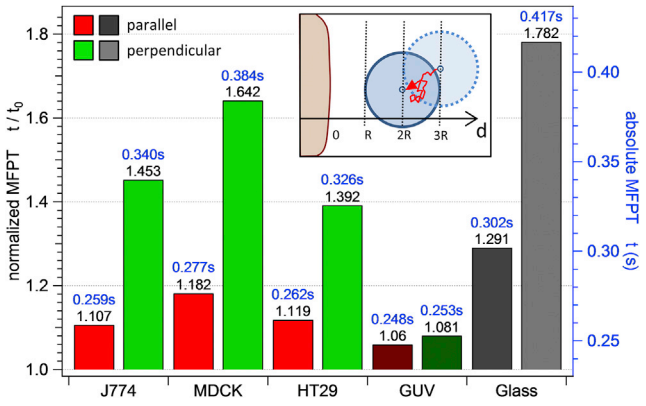

FIGURE 7 Anisotropic diffusion nearby interfaces. Mean first passage times $t_\perp(d_1,d_2)$ and $t_\parallel(d_1,d_2)$ for a 1 μm bead diffusing nearby an interface from $d_1 = 3R$ toward $d_2 = 2R$, as illustrated in the inset. Color coding is the same as in Fig. 6. To see this figure in color, go online.

accounting for this contact point uncertainty are presented in the Supporting Material; see Table S3 and Fig. S10.

To calculate the MFPTs at the glass interface, we performed a numerical integration of Eq. 5, where the term $\gamma_\infty + \gamma_0 e^{-(d-R)/\Lambda}$ was replaced by the respective approximation formula as given by Happel and Brenner (Eqs. 10 and 11). This analysis resulted in $t_{\parallel,Glass}(3R,2R) = 0.302$ s $= 1.291 \times t_0$ and $t_{\perp,Glass}(3R,2R) = 0.417$ s $= 1.782 \times t_0$. Those results are both even higher than those of all living cells, which is understandable, because the stiff character of the glass interface is expected to slow down the bead's diffusion more drastically than the presence of a flexible plasma membrane.

DISCUSSION

Short summary of the experimental results

In this study, we measured the diffusive behavior of 1 μm–sized particles in the vicinity of the plasma membranes of living cells, of a GUV, and a glass interface. We used a photonic force microscope equipped with a 3D interferometric tracking system, which allows us to record the Brownian motion of the particle at a 2 MHz sampling rate and with nanometer precision. By analyzing the short timescale diffusion via the AC of the particle's trajectory, we could observe and quantify a generally increased viscous drag near surfaces. For all cell types, the viscous drag perpendicular to the membrane is increased more significantly than in parallel direction. This behavior could not be observed for the GUV.

Accuracy of determining the bead-membrane-distance

Although the distance was reduced in steps of 20 nm, the relatively strong laser power restricted the bead diffusion to an area with radius of roughly 9 nm, both for parallel and perpendicular diffusion, which is less than 50% of the chosen step size. The piezo stage itself has a positioning accuracy of <1 nm. Because of this choice of parameters, the presence of the cell interface itself hardly influences the bead's fluctuations and therefore does not affect the results of the diffusion analysis. This is further supported by computer simulations shown in Figs. S4–S6.

The membrane of a living cell or a GUV is not rigid but is subject to thermal fluctuations. We have estimated the membrane fluctuations in two different ways: first, by trapping and calibrating the membrane in a weak laser focus and recording its thermal fluctuations analogously to the bead's motion as described in (53); second, by recording the fluctuations of a 1 μm bead that was bound to the membrane. Both methods gave an estimate that the membrane fluctuations are in the range of 4 nm, which is five times smaller than the step size, so that we can conclude that the role of the membrane fluctuations is negligible in this study.

However, because the PCM at the outside of the cell membrane gets first into contact with the bead, it might reduce the bead's position fluctuation width σ. In this way σ might drop off to 50% before the bead touches the membrane. Therefore, we estimated the latest-possible (worst-case) contact point, where the bead fluctuations reach a minimum σ_{min} of around typically 30% to 40% of the bulk value σ_0. The alternative contact point, where the bead fluctuation is minimal, is, in average, 0.22 μm $\pm$ 0.09 μm behind our initial contact estimate for the cells. It is likely that the true contact point between bead and cell membrane is in between these two estimates.

Reliability of the local viscous drag measurements

As described in the methods section, the values of the local viscous drag $\gamma(d)$ were obtained by the AC of the measured bead's trajectory on a short timescale of $\tau < 30$ μs. As the AC is calculated from a vast number of data points, corresponding to roughly 100 times the AC time τ_0, the results obtained from linear fitting are statistically reliable. Besides our short time analysis based on Eqs. 4 and 9, we have tested other methods to recover γ and κ, such as the analysis of the complete exponentially decaying AC, of the mean square displacement, or of the PSD. All methods yielded the same results for $\kappa_j(d)$ and $\gamma_j(d)$ (not shown). As mentioned above, the γ values extracted from $AC(\tau \ll \tau_0)$ coincide well with the theoretically predicted behavior of γ close to a glass surface according to Happel and Brenner. A frequency resolved analysis of $\gamma(\omega)$, shown in Fig. S12, reveals that $\gamma_j(d)$ has no relevant frequency-dependent contribution and that taking the average over all frequencies ω is justified. However, particle fluctuations nearby the cell membrane can be damped because of the PCM (glycocalyx) (8), which is not visible with DIC. This is possibly the reason for the decay of the perpendicular fluctuation width over a distance of ~0.2 μm in Fig. 3 *C* and the slight increase in the stiffness κ_y over the last 0.1 μm before cell contact as shown in Fig. 4 *A*. This length may be an indication for the thickness of the glycocalyx. Nevertheless, it is significantly shorter than the hydrodynamic decay length measured for several cells, the GUV, and the glass surface.

Influence of transient binding to the glycocalyx on the fluctuation data

Figs. 3 *B*, and 4 both contain hints that transient binding to the PCM can be identified in the fluctuation data. In Fig. 3 *B*, a drop of the fluctuation width in approach direction (y) can be observed already at roughly 250 nm before contact point (0,75 μm $> d >$ 0,5 μm), whereas the drop-off to 50% $\times \sigma_{0y}$ because of steric interaction between bead and cell is expected to take place only within one fluctuation width of

the bead, which is $\sigma_{0y} = 9{,}5$ nm in this study. This is further discussed in connection with Fig. S7.

It has been reported (8) that the PCM is not deformed or compressed by optically trapped beads passing though the PCM toward the cell membrane. Rather, the bead penetrates the PCM that thereon recovers in the vicinity of the bead. The transient binding to the PCM may reduce the fluctuation width as seen in Fig. 3 *B*, such that the drop to 50% of the bulk value σ_0 is reached before the actual contact with the cell membrane. By using an alternative estimate of the contact point, where σ_0 is reduced to the minimum width of ~$0.3\sigma_0$ to $0.4\sigma_0$, the hydrodynamic decay lengths $\Lambda_{\parallel}$ and $\Lambda_{\perp}$ are slightly decreased in average by 9% and 12%, respectively. At the same time, the viscous drags $\gamma_{0\parallel}$ and $\gamma_{0\perp}$ are increased in average by 40% to 63% and even 62% to 131% in the perpendicular case. However, even this worst-case estimation does not affect the overall analysis, data interpretation, and message of our study.

In Fig. 4, a rise of the stiffness parameter $\kappa_y(d)$ in approach direction of up to 20% is observed at roughly 0.1 μm before contact. Interaction with filopodia is unlikely according to the argumentation around Fig. 5, as there is no jump in $\gamma_y(d)$ (or in the parallel directions) at the same time. Also, Figs. S12 and S13 show sample approach traces for the glass interface and the GUV, which, in contrast to the cell approach, do not show a change in $\kappa_j(d)$ before the contact point.

Alongside Fig. S16, a passive microrheological analysis of the data in Fig. 4 is shown to estimate whether the transient binding to the PCM corrupts the measurement of $\gamma_j(d)$ and the associated hydrodynamic decay lengths. This becomes possible by calculating κ and γ from the real and imaginary part of the complex shear modulus, respectively, through the Kramers and Kronig relations. A comparison of the results obtained from AC analysis in Fig. 4 with the fluctuation range of the data obtained by microrheology (see Fig. S16) brings us to the conclusion that the determination of $\gamma_j(d)$ and Λ_j is still valid despite the apparent interaction of the bead with the PCM. Other studies, e.g., (8,51), show how bead-optical tweezers-assays can be used to probe the structure of the PCM, which is however beyond the scope of this study.

Error estimation for tracking nearby cells

As pointed out in the derivation of Eq. 9, the additional signal $S_{ic}(d)$ generated by the cell leads to an apparent additional particle displacement. This optical effect leads to a wedge function with axis intercept $\overline{b}_y^2$ adding up to the undisturbed AC and thereby slightly changing its slope and the resulting $\gamma(d)$. We roughly estimate from Fig. 3 *A* that the mean particle displacement is shifted by maximum $\overline{b}_y = 50$ nm when in close proximity to the cell membrane, which is a worst-case assumption, as the actual mean shift is always below 50 nm. It follows from geometrical considerations that the additional slope can be expressed as $\Delta AC/\tau_{max} = \overline{b}_y^2/\tau_{mes}$, where the linear part of the AC has been analyzed up to $\tau_{\max} = 30$ μs and $\tau_{\mathrm{mes}} = 150$ ms represents the measurement time at a distance d. Given these values, Eqs. 3 and 9 together with $\overline{b}_y^2 = S_{ic,y}(d \approx R)^2/g_y^2$ then provide an upper limit estimate of the systematic error: $(k_BT/\gamma^*_{max}) = (k_BT/\gamma_{max}) + (\overline{b}_y^2/\tau_{mes})$. Assuming $\gamma_{max} = \gamma_{\infty} = 8.0 \times 10^{-9}$ Ns/m results in $\Delta\gamma_{max} = -2.4 \times 10^{-10}$ Ns/m, which is only 3.0% of γ_{∞} (with $\Delta\gamma_{max} = \gamma^*_{max} - \gamma_{max}$). In conclusion, the systematic error originating from the additional signal $S_{ic}(d)$ is negligibly small in the short-time AC analysis based on Eqs. 3 and 9.

Suitability of the exponential model

Our simplified assumption of the exponentially decaying viscous drag for decreasing distance between the particle and the cell membrane fits remarkably well to our measurement data. It offers the great advantage that the changing hydrodynamics at smooth interfaces such as the lipid membranes of different cells or of artificial vesicles can be described by just two quantities, the maximum viscous drag γ_{0j} and the hydrodynamic decay length Λ_j. Furthermore, a comparison between viscosities at different interfaces becomes easily possible.

However, the exponential decay fails to give a correct approximation of the diffusive behavior of a bead close to a glass interface. In the right inset of Fig. 6 *A*, the deviation of the data points from the exponential behavior can be seen, which may lead to a misinterpretation of the calculated hydrodynamic decay lengths and MFPT for glass. A realistic estimation of the MFPTs at glass interfaces could be achieved by the numerical integration of Eq. 5 as discussed in the results section. Calculation of the MFPTs at the glass interface by using the approach of Eqs. 2 and 5 would result in $t_{\parallel}(3R,2R) = 1.016 \times t_0$ and $t_{\perp}(3R,2R) = 1.024 \times t_0$, which is unrealistically low because of the non-exponential increase of $\gamma_j(d)$ at a glass interface. The realistic results ($t_{\parallel,Glass}(3R,2R) = 0.302$ s $= 1.291 \times t_0$ and $t_{\perp,Glass}(3R,2R) = 0.417$ s $= 1.782 \times t_0$) for the MFPT, which are given in the results section, are in fact significantly higher than $t_{\parallel}(3R,2R) = 1.016 \times t_0$ and $t_{\perp}(3R,2R) = 1.024 \times t_0$.

The increase of the static viscous drag close to a plane membrane separating two identical fluids as predicted theoretically by Lee et al. (13,14) and Bickel (15,16) is of the form $\gamma(d)/\gamma_0 = (1 - \alpha \times (R/d))^{-1}$ and does not resemble an exponentially decaying function (α is a constant and R is the sphere radius). However, a bead close to a spherical surface—like it is the case for our cells—can drag the water more easily to the side, compared with the case of a plane surface. Therefore, one can expect a less-steep increase in viscous drag close to a spherical surface, which could partly explain the difference between our measured curves and the theoretical predictions for the static viscous drag. However,

further investigations are required to model the decay of the viscous drag considering dynamic effects, nonplane and elastic membranes, as well as different viscosities on both sides of the membrane.

Anisotropy of hydrodynamic decay lengths for living cells

All measurements performed on cells show the common result that the hydrodynamic decay lengths in perpendicular direction are significantly longer than in parallel direction. This behavior cannot be seen with the GUV, where $\Lambda_\perp$ and $\Lambda_\parallel$ are of comparable length. Interestingly, GUVs and cells, which both have a phospholipid bilayer membrane, show the same decay lengths of $\Lambda_\parallel \approx 0.3\ \mu$m for parallel diffusion.

A possible physical explanation for a significantly stronger increase in viscous drag for perpendicular diffusion could be the following: without an interface, the hydrodynamic drag can be transferred from one particle to another via the surrounding fluid, depending on the distance (10,54). A transfer of hydrodynamic momentum through an interface is also possible, if the interface can deform and relax its shape or can transmit fluid molecules to a certain extent. Lipid membranes behave like this, and therefore can transfer hydrodynamic momentum from the outside of the GUV to its interior, i.e., in normal direction equally well as in lateral direction. In front of a stiff wall the hydrodynamic drag cannot be transferred anymore, which leads to a local fluid compression. In consequence, the motion of a bead is hindered and damped, leading to a strong increase in viscosity; see Fig. 6 *B*. Simply because of geometric constraints, it is obvious that the fluid can be dragged more easily parallel to the interface than in direction to the interface. This coincides with the theoretical prediction that the normal component of the viscous drag close to a glass surface increases to infinity with decreasing distance according to the theory of Happel and Brenner, i.e., $\gamma_{0\perp} \rightarrow \infty$, but also diverges in the experiments. Unlike solid surfaces, lipid membranes behave like two-dimensional fluids and a hydrodynamic drag from the environment can result in lateral membrane motion, thus reducing friction in parallel direction.

The hydrodynamic momentum produced by the drag of the sphere is completely repelled at a stiff interface, thus doubling the amount of mechanical momentum taken up by the stiff medium. A thin elastic membrane transfers most of the incoming momentum without significant repulsion. Cells represent an intermediate case, where part of the momentum is transferred and the other part is repelled, leading to an increase in viscous drag with a specific decay length. This hydrodynamic coupling length is the distance within which the momentum transfer to the interface starts to increase relative to the case of a homogeneous fluid.

At the cell membranes, the perpendicular drag coefficients $\gamma_{0\perp} = 5.1 \times \gamma_\infty$ (J774) and $\gamma_{0\perp} = 6.2 \times \gamma_\infty$ (HT29) are five to six times larger than the bulk value $\gamma_\infty = 8.0 \times 10^{-9}$ Ns/m, whereas the increase in viscous drag close to a GUV membrane is fundamentally smaller ($\gamma_{0\perp} = 1.10 \times \gamma_\infty$). In other words, momentum transfer through a membrane is better possible, if the fluid on both sides of the membrane is approximately the same regarding viscosity and osmolarity, as in the case of the GUV. However, the situation is different with living cells, because the plasma membrane exhibits a more complex composition of different lipids and lipid rafts, pores, and membrane proteins, many of them linked to the cytoskeleton (55). The interior of the cell is crowded with vesicles, macromolecules, cytoskeletal filaments, organelles, and other membranes, resulting in a higher density and a more rigid structure that apparently dampens the transfer of hydrodynamic momentum. The difference in $\gamma_{0\perp}$ for different cell types is probably a result of different compositions of the cell interior and also of the PCM, both because of the different functions of these cell types.

Our calculations show that the MFPTs are also influenced, as shown in Fig. 7. For a sphere diffusing over $R = 0.5\ \mu$m toward the cell from distance $d_1 = 3R$ toward $d_2 = 2R$, the parallel MPFTs are hardly changed. In perpendicular direction, however, the MPFT is increased significantly by 30% to 65%. These times become the longer, the closer the particle approaches the cell.

Biological interpretation

The hydrodynamic coupling of the approaching particle in perpendicular direction exerts a hydrodynamic pressure, i.e., momentum transfer, onto the cell, which, in consequence, must apply a force to the membrane and mechano-sensitive proteins therein. The pronounced increase in viscous drag slows down the particle's diffusion and thus reduces the rate of collisions with membrane components and thereby reduces the interaction probability in a given time window. The denser and more viscous the cell, the more hydrodynamic momentum is transferred to its interior, but the more the mobility and the collision rate are reduced outside the cell. The reduced collision rate corresponds to a limited temporal bandwidth of information (momentum) transfer. In this way, less broad-band noise is transferred to the cell. Thereby, the local increase of viscosity leads to a low-pass filtering of incoming signals, and one may conclude that only distinct, pronounced momentum changes can be transferred to the cell interior.

For example, as a response to the hydrodynamic pressure of the particle, the cell can reorganize the cytoskeleton connected to the membrane or can initiate the growth of cell protrusions such as filopodia.

The larger parallel mobility compared with the bead's perpendicular motion allows a particle to diffuse faster parallel to the membrane and to better find specific or unspecific binding sites across the cell surface. Because the particle fluctuations are faster in parallel than in

perpendicular direction, also the particle's collision rate is higher in parallel direction. This might, for example, help cells to improve their endocytosis efficiency by a facilitated search of the particle for membrane binding sites.

CONCLUSIONS

The viscosity of a fluid determines the mobility of a particle on a macroscopic scale and the dissipation of particle fluctuations on a microscopic scale. Close to different cellular interfaces, this behavior changes strongly—an effect that can significantly influence the probability of particle binding to the interface. Using a photonic force microscope with a fast 3D interferometric particle tracking system, we show for the first time, to our knowledge, that the viscous drag increases nearly exponentially with decreasing distance to the membranes of living cells and of GUVs. Similar to the direction-dependent changes of the viscosity nearby stiff interfaces, but nevertheless unexpected, we found that three different types of cells show a significantly stronger increase in viscosity in perpendicular direction than in parallel direction. However, all three different cells and the GUVs are characterized by a strongly different hydrodynamic coupling length and maximum viscosity, which we believe are a consequence of the cell's composition and its regulation of proteins and lipids inside the cell or the membrane and also the PCM. It is remarkable that the correlation of the particle position fluctuations encode the cellular membrane composition and the ability to transfer information. However, further investigations need to uncover the relation between the cellular constituents near the membrane, the hydrodynamic coupling length and strength outside the membrane, and the connected physiological function. Fast particle fluctuations, as measurable by photonic force microscopy, encode a lot of relevant information to understand the molecular processes of endocytosis or drug delivery.

SUPPORTING MATERIAL

Supporting Material, sixteen figures, and three tables are available at http://www.biophysj.org/biophysj/supplemental/S0006-3495(15)00734-1.

AUTHOR CONTRIBUTIONS

F.J. performed cell experiments, analyzed and interpreted the data, and prepared the figures; F.K. designed and constructed the microscope setup; A.M. performed GUV experiments; T.M. developed the BD simulation framework; R.N. and B.E. provided and prepared the cells; and A.R. initiated and supervised the project, obtained financial funding, interpreted the data, and wrote the manuscript together with F.J.

ACKNOWLEDGMENTS

The authors gratefully acknowledge fruitful discussion with Dr. Andreas Greiner and financial funding from the Deutsche Forschungsgemeinschaft (DFG), grant RO 3615/3-1.

SUPPORTING CITATIONS

References (56–60) appear in the Supporting Material.

REFERENCES

1. Wang, Y., E. L. Botvinick, …, S. Chien. 2005. Visualizing the mechanical activation of Src. *Nature.* 434:1040–1045.
2. Escudé, M., M. K. Rigozzi, and E. M. Terentjev. 2014. How cells feel: stochastic model for a molecular mechanosensor. *Biophys. J.* 106:124–133.
3. Gordon, S. 2007. The macrophage: past, present and future. *Eur. J. Immunol.* 37 (*Suppl. 1*):S9–S17.
4. Wynn, T. A., A. Chawla, and J. W. Pollard. 2013. Macrophage biology in development, homeostasis and disease. *Nature.* 496:445–455.
5. Peetla, C., S. Jin, …, V. Labhasetwar. 2014. Biomechanics and thermodynamics of nanoparticle interactions with plasma and endosomal membrane lipids in cellular uptake and endosomal escape. *Langmuir.* 30:7522–7532.
6. Timko, B. P., K. Whitehead, …, R. Langer. 2011. Advances in drug delivery. *In* Annual Review of Materials Research. D. R. Clarke and P. Fratzl, editors. Annual Reviews, Palo Alto, CA, pp. 1–20.
7. Tiwari, G., R. Tiwari, …, S. K. Bannerjee. 2012. Drug delivery systems: an updated review. *Int. J. Pharm. Investig.* 2:2–11.
8. McLane, L. T., P. Chang, …, J. E. Curtis. 2013. Spatial organization and mechanical properties of the pericellular matrix on chondrocytes. *Biophys. J.* 104:986–996.
9. Kress, H., E. H. K. Stelzer, …, A. Rohrbach. 2005. Control of relative radiation pressure in optical traps: application to phagocytic membrane binding studies. *Phys. Rev. E Stat. Nonlin. Soft Matter Phys.* 71:061927.
10. Traenkle, B., M. Speidel, and A. Rohrbach. 2012. Interaction dynamics of two colloids in a single optical potential. *Phys. Rev. E Stat. Nonlin. Soft Matter Phys.* 86:021401.
11. Thomas, D. N., S. J. Judd, and N. Fawcett. 1999. Flocculation modelling: a review. *Water Res.* 33:1579–1592.
12. Happel, J., and H. Brenner. 1963. Low Reynolds Number Hydrodynamics with Special Applications to Particulate Media. Prentice-Hall, Englewood Cliffs, NJ.
13. Lee, S. H., R. S. Chadwick, and L. G. Leal. 1979. Motion of a sphere in the presence of a plane interface. Part 1. An approximate solution by generalization of the method of Lorentz. *J. Fluid Mech.* 93:705–726.
14. Lee, S. H., and L. G. Leal. 1980. Motion of a sphere in the presence of a plane interface. Part 2. An exact solution in bipolar co-ordinates. *J. Fluid Mech.* 98:192–224.
15. Bickel, T. 2006. Brownian motion near a liquid-like membrane. *Eur. Phys. J. E Soft Matter.* 20:379–385.
16. Bickel, T. 2007. Hindered mobility of a particle near a soft interface. *Phys. Rev. E Stat. Nonlin. Soft Matter Phys.* 75:041403.
17. Faucheux, L. P., and A. J. Libchaber. 1994. Confined Brownian motion. *Phys. Rev. E Stat. Phys. Plasmas Fluids Relat. Interdiscip. Topics.* 49:5158–5163.
18. Bevan, M. A., and D. C. Prieve. 2000. Hindered diffusion of colloidal particles very near to a wall: revisited. *J. Chem. Phys.* 113:1228–1236.
19. Clapp, A. R., and R. B. Dickinson. 2001. Direct measurement of static and dynamic forces between a colloidal particle and a flat surface using a single-beam gradient optical trap and evanescent wave light scattering. *Langmuir.* 17:2182–2191.
20. Holmqvist, P., J. K. G. Dhont, and P. R. Lang. 2006. Anisotropy of Brownian motion caused only by hydrodynamic interaction with a wall. *Phys. Rev. E Stat. Nonlin. Soft Matter Phys.* 74:021402.
21. Pralle, A., E. L. Florin, …, J. K. H. Hörber. 1998. Local viscosity probed by photonic force microscopy. *Appl. Phys. A Mater. Sci. Process.* 66 (*Suppl.*):S71–S73.

22. Schäffer, E., S. F. Nørrelykke, and J. Howard. 2007. Surface forces and drag coefficients of microspheres near a plane surface measured with optical tweezers. *Langmuir.* 23:3654–3665.
23. Benmouna, F., and D. Johannsmann. 2002. Hydrodynamic interaction of AFM cantilevers with solid walls: an investigation based on AFM noise analysis. *Eur. Phys. J. E Soft Matter.* 9:435–441.
24. Joly, L., C. Ybert, and L. Bocquet. 2006. Probing the nanohydrodynamics at liquid-solid interfaces using thermal motion. *Phys. Rev. Lett.* 96:046101.
25. Hansen, P. M., J. K. Dreyer, …, L. Oddershede. 2005. Novel optical and statistical methods reveal colloid-wall interactions inconsistent with DLVO and Lifshitz theories. *J. Colloid Interface Sci.* 287: 561–571.
26. Pralle, A., E.-L. Florin, …, J. K. H. Hörber. 2000. Photonic force microscopy: a new tool providing new methods to study membranes at the molecular level. *Single Molec.* 1:129–133.
27. Dufresne, E. R., T. M. Squires, …, D. G. Grier. 2000. Hydrodynamic coupling of two Brownian spheres to a planar surface. *Phys. Rev. Lett.* 85:3317–3320.
28. Meiners, J.-C., and S. R. Quake. 1999. Direct measurement of hydrodynamic cross correlations between two particles in an external potential. *Phys. Rev. Lett.* 82:2211–2214.
29. Ruh, D., B. Tränkle, and A. Rohrbach. 2011. Fast parallel interferometric 3D tracking of numerous optically trapped particles and their hydrodynamic interaction. *Opt. Express.* 19:21627–21642.
30. Bolognesi, G., S. Bianchi, and R. Di Leonardo. 2011. Digital holographic tracking of microprobes for multipoint viscosity measurements. *Opt. Express.* 19:19245–19254.
31. Lutz, C., M. Reichert, …, C. Bechinger. 2006. Surmounting barriers: the benefit of hydrodynamic interactions. *Europhys. Lett.* 74:719–725.
32. Speidel, M., L. Friedrich, and A. Rohrbach. 2009. Interferometric 3D tracking of several particles in a scanning laser focus. *Opt. Express.* 17:1003–1015.
33. Tränkle, B., and A.Rohrbach. Interaction probability of two diffusing particles. Contact times and influence of nearby surfaces. *Soft Matter.* Submitted.
34. Tränkle, B., M. Speidel, and A. Rohrbach. 2012. Interaction dynamics of two colloids in a single optical potential. *Phys. Rev. E Stat. Nonlin. Soft Matter Phys.* 86:021401.
35. Tischer, C., S. Altmann, …, E.-L. Florin. 2001. Three-dimensional thermal noise imaging. *Appl. Phys. Lett.* 79:3878–3880.
36. Florin, E.-L., A. Pralle, …, J. K. H. Hörber. 1998. Photonic force microscope calibration by thermal noise analysis. *Appl. Phys. A Mater. Sci. Process.* 66 (*Suppl.*):S75–S78.
37. Tischer, C., A. Pralle, and E.-L. Florin. 2004. Determination and correction of position detection nonlinearity in single particle tracking and three-dimensional scanning probe microscopy. *Microsc. Microanal.* 10:425–434.
38. Meinel, A., B. Tränkle, …, A. Rohrbach. 2014. Induced phagocytic particle uptake into a giant unilamellar vesicle. *Soft Matter.* 10:3667–3678.
39. Coffey, W. T., P. Kalmykov Yu, and J. T. Waldron. 1996. The Langevin equation: with applications in physics, chemistry and electrical engineering. World Scientific, Singapore.
40. Griesshammer, M., and A. Rohrbach. 2014. 5D-tracking of a nanorod in a focused laser beam—a theoretical concept. *Opt. Express.* 22:6114–6132.
41. Rohrbach, A., C. Tischer, …, E. H. K. Stelzer. 2004. Trapping and tracking a local probe with a photonic force microscope. *Rev. Sci. Instrum.* 75:2197–2210.
42. Seitz, P. C., E. H. K. Stelzer, and A. Rohrbach. 2006. Interferometric tracking of optically trapped probes behind structured surfaces: a phase correction method. *Appl. Opt.* 45:7309–7315.
43. Dreyer, J. K., K. Berg-Sørensen, and L. Oddershede. 2004. Improved axial position detection in optical tweezers measurements. *Appl. Opt.* 43:1991–1995.
44. Friedrich, L., and A. Rohrbach. 2012. Tuning the detection sensitivity: a model for axial backfocal plane interferometric tracking. *Opt. Lett.* 37:2109–2111.
45. Rohrbach, A., and E. H. K. Stelzer. 2002. Three-dimensional position detection of optically trapped dielectric particles. *J. Appl. Phys.* 91:5474–5488.
46. Seitz, P. C. 2005. Messung und simulation von wechselwirkungen an oberflächen mit optisch gefangenen partikeln. *In* Fakultät für Physik und Astronomie. Ruprecht-Karls-Universität Heidelberg, Heidelberg, Germany.
47. Kress, H., E. H. K. Stelzer, …, A. Rohrbach. 2007. Filopodia act as phagocytic tentacles and pull with discrete steps and a load-dependent velocity. *Proc. Natl. Acad. Sci. USA.* 104:11633–11638.
48. Zidovska, A., and E. Sackmann. 2011. On the mechanical stabilization of filopodia. *Biophys. J.* 100:1428–1437.
49. Knöner, G., B. E. Rolfe, …, H. Rubinsztein-Dunlop. 2006. Mechanics of cellular adhesion to artificial artery templates. *Biophys. J.* 91:3085–3096.
50. Cohen, M., E. Klein, …, L. Addadi. 2003. Organization and adhesive properties of the hyaluronan pericellular coat of chondrocytes and epithelial cells. *Biophys. J.* 85:1996–2005.
51. Chenevier, P., B. Veyret, …, N. Henry-Toulmé. 2000. Interaction of cationic colloids at the surface of J774 cells: a kinetic analysis. *Biophys. J.* 79:1298–1309.
52. Bacabac, R. G., T. H. Smit, …, J. Klein-Nulend. 2005. Dynamic shear stress in parallel-plate flow chambers. *J. Biomech.* 38:159–167.
53. Gögler, M., T. Betz, and J. A. Käs. 2007. Simultaneous manipulation and detection of living cell membrane dynamics. *Opt. Lett.* 32:1893–1895.
54. Leckband, D., and J. Israelachvili. 2001. Intermolecular forces in biology. *Q. Rev. Biophys.* 34:105–267.
55. Alberts, B., A. Johnson, …, P. Walter. 2004. Essential Cell Biology. Garland Publishing, New York.
56. Buchanan, M., M. Atakhorrami, …, C. F. Schmidt. 2005. High-frequency microrheology of wormlike micelles. *Phys. Rev. E Stat. Nonlin. Soft Matter Phys.* 72:011504.
57. Gittes, F., B. Schnurr, …, C. F. Schmidt. 1997. Microscopic viscoelasticity: shear moduli of soft materials determined from thermal fluctuations. *Phys. Rev. Lett.* 79:3286–3289.
58. Grassia, P. S., E. J. Hinch, and L. C. Nitsche. 1995. Computer simulations of Brownian motion of complex systems. *J. Fluid Mech.* 282:373–403.
59. Landau, L. D., and E. M. Lifshitz. 1969. Statistical Physics. Pergamon Press, Oxford, UK.
60. Schnurr, B., F. Gittes, …, C. F. Schmidt. 1997. Determining microscopic viscoelasticity in flexible and semiflexible polymer networks from thermal fluctuations. *Macromolecules.* 30:7781–7792.

Supporting Information to

Measuring Local Viscosities near Plasma Membranes of Living Cells with Photonic Force Microscopy

Felix Jünger,[†] Felix Kohler,[†] Andreas Meinel,[†] Tim Meyer,[‡] Roland Nitschke,[§] Birgit Erhard,[†] and Alexander Rohrbach,[†]*

[†]Laboratory for Bio- and Nano-Photonics, Department of Microsystems Engineering, University of Freiburg, Germany

[‡]Macromolecular Modelling Group, Institute of Chemistry and Biochemistry, Freie Universität Berlin, Germany

[§]Life Imaging Center (LIC) and Center for Biological Systems Analysis (ZBSA), University of Freiburg, Germany

[*]Correspondence: rohrbach@imtek.de

Estimation of the effect of the membrane curvature on the distance-dependent viscous drag

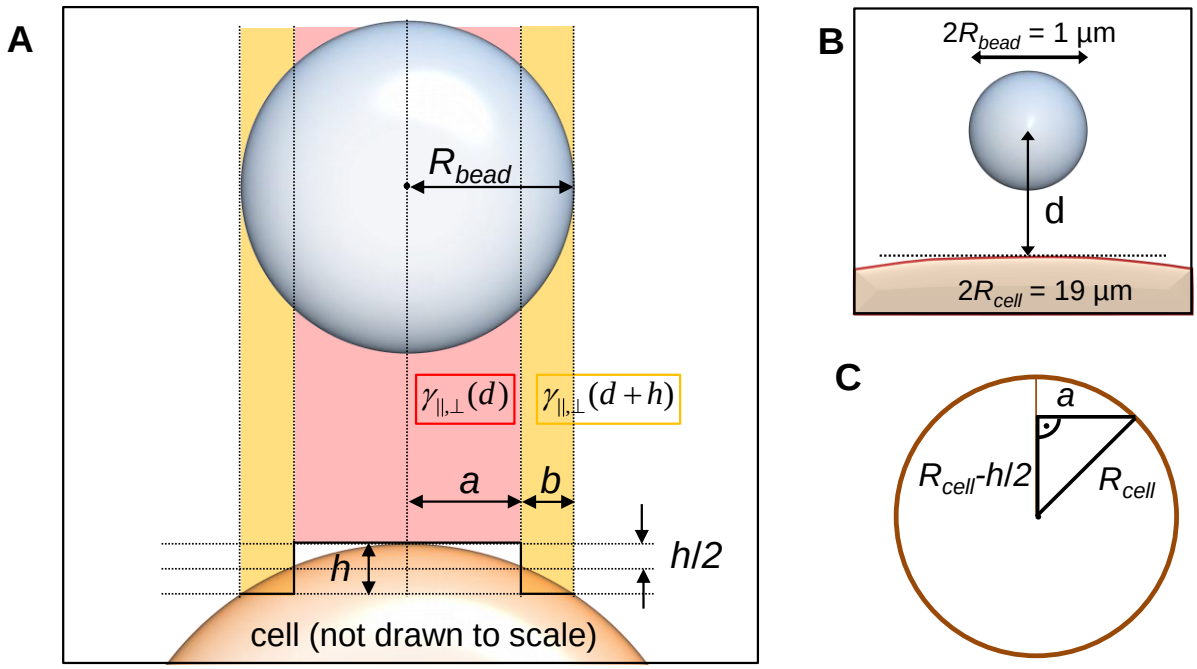

FIGURE S1 Estimated effect of the cell's curvature on the viscous drag $\gamma(d)$ close to interfaces. (A) The curvature is modeled by a stepped function with heights h and step widths a and $b = R-a$, respectively. This leads to different distances of the projected bead center to the curved surface, indicated by the red and yellow shaded regions. (B) Sketch of the actual geometry, cell and bead are drawn to scale. (C) The step height h defines the step width a with regard to the cell's radius of curvature R_{cell}.

Although the cell's radius of curvature is large compared to the bead radius, the cell membrane is not perfectly flat but exhibits a certain, albeit marginal, curvature. Here, an estimation of the effect of the curvature on the measured distance-dependent viscous drag is made. In a very simple approach, the curved cell membrane is approximated by a stepped function consisting of two steps with widths a and $b = R-a$, respectively, separated by a vertical distance h, as depicted in Fig. S1 *A*. For better visibility, the sketch in Fig. S1 *A* is not drawn to scale, a properly scaled sketch is shown in Figure S1 *B* with R_{bead} = 0.5 µm and R_{cell} = 9.5 µm as deducted from Fig. 2 in the main text. The step height h and its width $2a$ are related to each other via the cell's radius of curvature R_{cell} and can be calculated by the Pythagorean theorem $(R_{cell}-h)^2+a^2=R_{cell}^{\ 2}$, see Fig. S1 *C*. If the step is chosen to intersect the circular arc representing the cell membrane at its half height $h/2$, it immediately follows that a = 354 nm and h = 12.5 nm. This leads to the approach of superposed distances weighted by the geometrical overlap (projection) of the bead diameter with the cell surface. In terms of the spatially varying viscous drag $\gamma(d)$, the measured viscous drag has to be considered as an average of different $\gamma(d')$ corresponding to superposed distances d' between bead center and surface, each weighted by the part of the bead that sees the respective distance d'.

In our step-like approximation, the relation for the averaged $\bar{\gamma}_{\parallel,\perp}$ reads as follows:

$$\bar{\gamma}_{\parallel,\perp} = \frac{a}{R} \cdot \gamma_{\parallel,\perp}(d) + \frac{b}{R} \cdot \gamma_{\parallel,\perp}(d+h) \tag{S1}$$

The weighting factors a/R and b/R = 1-a/R correspond to the ratio of twice the surface of a spherical cap with height b ($A_{cap} = 2\pi Rb$) and the surface of the remaining sphere ($A_{rest} = 4\pi R^2 - 2A_{cap}$):

$$\frac{2A_{cap}}{A_{sphere}} = \frac{4\pi Rb}{4\pi R^2} = \frac{b}{R} \qquad \text{and} \qquad \frac{A_{rest}}{A_{sphere}} = \frac{4\pi R^2 - 4\pi Rb}{4\pi R^2} = \frac{R-b}{R} = \frac{a}{R} \tag{S2}$$

The bead fluctuations $\sigma_{\parallel,\perp}$ = 9.5 nm, which are only 1 % of the bead's diameter, are neglected in this calculation.

In the following, sample curves $\bar{\gamma}_{\parallel,\perp}(d)$ that are corrected according to Eq. S1 are presented and the deviation from the uncorrected curves is discussed. In Fig. S2 *A*, theoretical curves $\gamma_{\parallel,\perp}(d)$ according to Happel's and Brenner's formulas (see main text) are shown together with the corrected curves $\bar{\gamma}_{\parallel,\perp}(d)$ accounting for the geometrical circumstances as shown above. The same analysis is performed for $\gamma_{\parallel,\perp}(d)$ of a 1 µm bead close to a HT29 cell in Fig. S2 *B*. The curves were modeled according to Eq. 2 in the main text with the parameters obtained in the results section, i.e., $\gamma_{0\perp} = 6.23 \times \gamma_\infty$ and $\Lambda_\perp = 0.45$µm in perpendicular direction (green data) and $\gamma_{0\parallel} = 2.80 \times \gamma_\infty$ and $\Lambda_\parallel = 0.28$ µm parallel to the interface (red data).

The original curves $\gamma_{\parallel,\perp}(d)$ (solid lines) and the curves $\bar{\gamma}_{\parallel,\perp}(d)$ (dotted lines) corrected for the curvature of the interface can hardly be separated in the left part of Fig. S2, indicating that the effect of the curvature on the measured $\gamma_{\parallel,\perp}(d)$ is small. The insets with numbers 1 and 2 show magnifications of both curves close to the contact point at $d = R$, where the small deviation of both curves becomes apparent. To quantitatively estimate this effect, the $\gamma_{\parallel,\perp}(d = R)$ values and $\bar{\gamma}_{\parallel,\perp}(d = R)$ values are given in the figure insets together with the deviation Δ of these numbers in percent. It can be seen that the deviation in the given geometry is in the range of 0.5% for the HT29 cell model curve and 2.5% for the stiff glass interface. Due to the fact that $\gamma_\perp(d)$ diverges for $d \to R$ in the latter case, a mathematical estimation for Δ is only available for the parallel data.

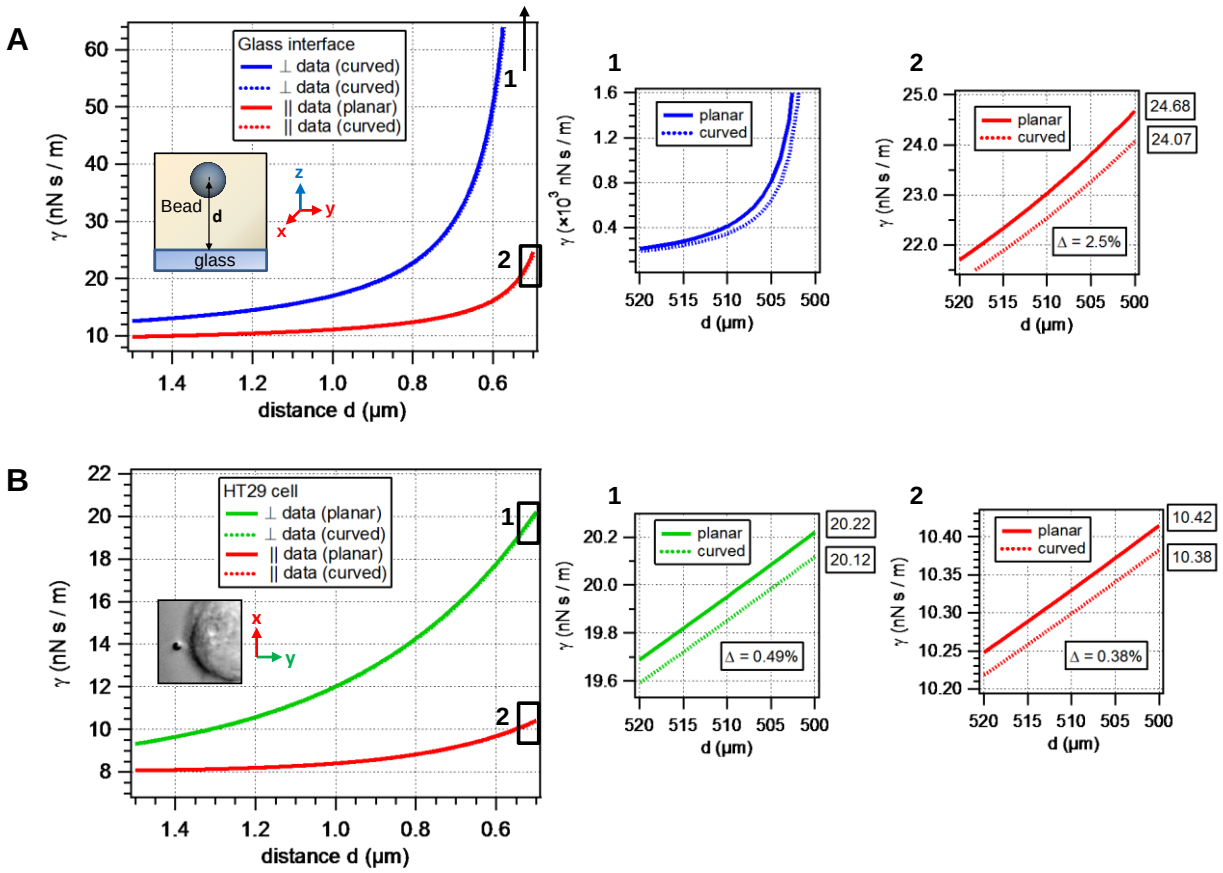

FIGURE S2 Distance-dependent viscous drag $\gamma(d)$ close to a flat (solid lines) and a curved surface (dotted lines). Both curves can hardly be separated, in the insets showing the last 20 nm before contact (d=R) the deviation of both curves of only 0.38% - 2.5% becomes apparent. (A) Case of a bead approaching a stiff planar wall according to Happel's and Brenner's formula. Blue curves correspond to the direction perpendicular to the interface, red to the parallel direction. (B) $\gamma(d)$ for a bead approaching a HT29 modeled by the parameters from the results section. Green data = perpendicular, red = parallel direction. The corrected data represents our estimate for a slightly curved cell surface.

Note that due to the oversimplification of the actual geometry as discussed above, these calculations represent only an estimate of the effect of the cell's curvature rather than a mathematically exact formulation. Nevertheless, the observed order of magnitude of this effect suggests that the curvature of the cell membrane has only a minor effect on the measured viscous drag and can therefore be neglected. For the vertical cell radius of about R_{cell} = 7.5 µm, the deviation of the corrected curve would be Δ = 3.1% instead of 2.5% and, e.g., R_{cell} = 2 µm would result in Δ = 7.9% (not shown).

QPD data recording in the proximity of the cell membrane

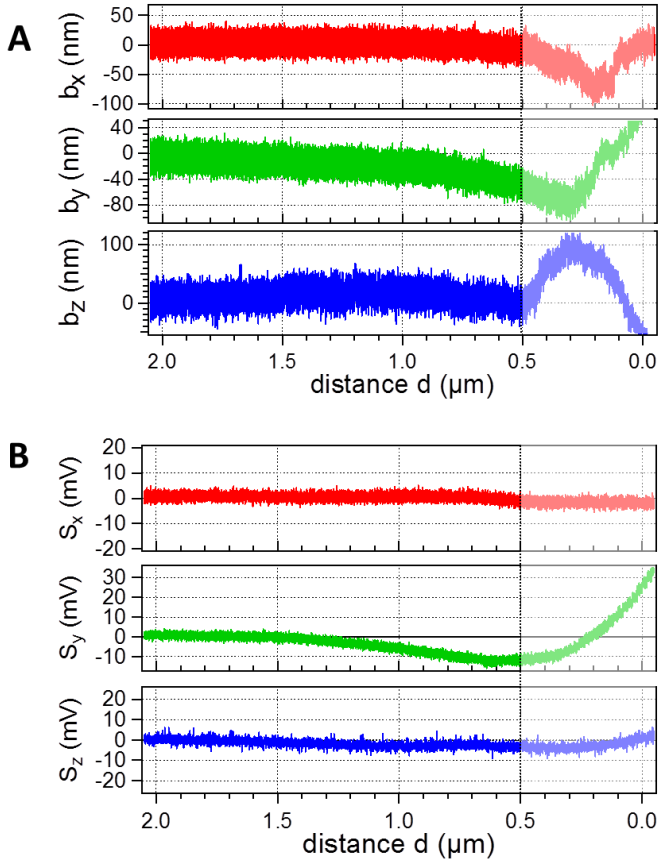

FIGURE S3 Fluctuation data close to a cell membrane. (A) Distance-dependent position trajectories $b_x(d,t)$, $b_y(d,t)$, $b_z(d,t)$ of a 1 µm sized bead approaching the membrane of a HT29 cell, calculated from the QPD data after calibration. *y* data correspond to scan direction. Bead surface and cell membrane are in contact for $d \leq R$ (masked by semi-transparent boxes). (B) QPD voltage signals of a laser focus without trapped bead are recorded upon approaching the same cell at the same site with the same parameters.

The acquisition of the QPD voltage signals and their conversion into bead position trajectories $b_x(t)$, $b_y(t)$, $b_z(t)$ via calibration is described in the main text. Figure S3 *A* shows the same data as Fig. 3 *A* together with voltage signals of an empty trap approaching the same cell on the same approach line, see Fig. S3 *B*. This control measurement allows us to estimate purely optical effects as no bead fluctuations are measured. The decrease in the *y* signal before cell contact, apparent in Figs. 3 *A* and S3 *A*, respectively, is also visible in Fig. S3 *B* and confirms the signal slope in Fig. 3 *A* (green curve) and the theoretical approach in Eq. 8. It furthermore proves that this effect must not be confused with the (small) shift of the bead trajectory's mean position due to mechanical interaction (contact) with the cell interface. The latter occurs on a much shorter length scale, namely one fluctuation width before surface contact (approximately 9 nm), compared to roughly 0.7 µm before contact deduced from Figs. 3 *A* and S3. The mechanical effect is revisited in the discussion in the main text and in the context of Fig. S5.

Computer simulations of a 1 µm bead's Brownian motion close to an interface

To study the influence of the interface on the bead's fluctuation data, Brownian dynamics (BD) simulations based on the Langevin equation were performed in addition to the experiments presented in this study. Details of the simulation algorithm can be found in (1). In brief, the bead's diffusive motion is simulated by adding a random displacement to the bead's trace $b_j(t)$ at each time step ($j = x,y,z$). The random numbers are chosen such that their temporal mean value equals zero and that the mean squared displacement $\langle (b_j(t+\tau) - b_j(t))^2 \rangle = 2D \cdot \tau$ grows linearly as expected for the free diffusion of the particle (2).

The motion of a $2R$ = 1 µm polystyrene bead in a harmonic optical trap potential with isotropic force constants κ_j = 50 pN/µm for all $j = x,y,z$ in watery solution at temperature T = 37°C was simulated. The theoretical fluctuation width according to the equipartition theorem is $\sigma_j = (kT/\kappa_j)^{0.5}$ = 9.2 nm. An obstacle in form of a rigid, infinitely large surface was introduced in y direction and subsequently approached toward the trap center in distinct steps (Δy = 4 nm for $d\text{-}R \leq 40$ nm, Δy = 10 nm for $d\text{-}R > 40$ nm). For the sake of simplicity, the distance-dependent change in viscous drag as described by Happel and Brenner was neglected in the simulation, such that $\gamma_j(d) = \gamma_\infty = 8.0 \times 10^{-9}$ Ns/m remained constant. All simulation parameters were chosen to meet the experimental conditions. The standard deviation $\sigma_y(t)$ of the bead's fluctuations in perpendicular direction was roughly 9 nm as also measured in the experiments.

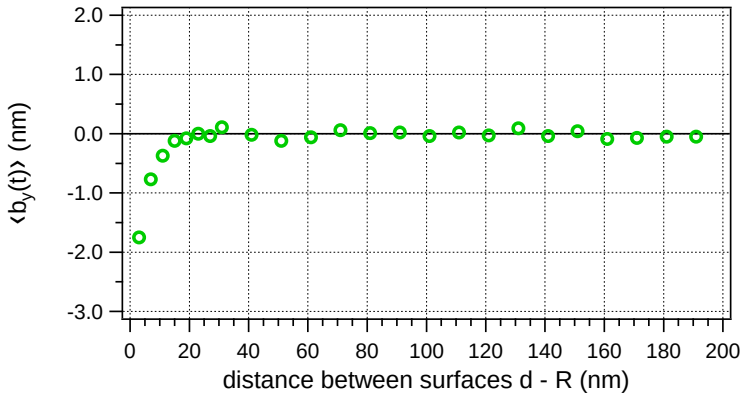

FIGURE S4 BD simulation: The mean position value $\langle b_y(t) \rangle$ of a $2R$ = 1 µm bead's diffusive motion hardly changes close to a rigid surface.

Due to short contacts of the fluctuating bead with the interface, the fluctuation volume becomes slightly asymmetric and shifts the mean value of the position histogram. Figure S4 reveals that the presence of the interface leads to a slight decrease of the mean bead's displacement $\langle b_y(t) \rangle$, which, however, only appears at distances smaller than the bead's fluctuation width, i.e., $d\text{-}R < 9$ nm. For any larger distance, the mean value remains constantly zero. This effect must not be confused with the shift of the signal that occurs due to additional light scattering at the cell, as it was discussed following Eq. 8 in the main text. Since the piezo step size in the

experiments was chosen larger than $\sigma_y(t)$ and only data points at distances d-R > 0 were considered for data analysis, this effect does not affect the data presented in this study.

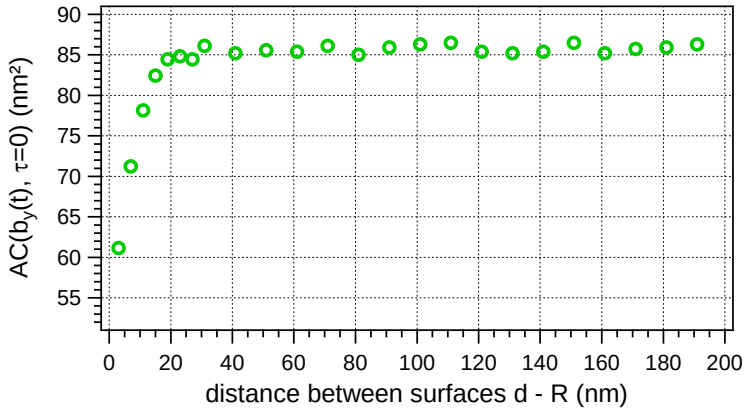

FIGURE S5 BD simulation: Distance-dependent variance $\langle b_y(t)^2 \rangle = AC(\tau=0)$ of a $2R$ = 1µm bead's diffusive motion perpendicular to a rigid surface.

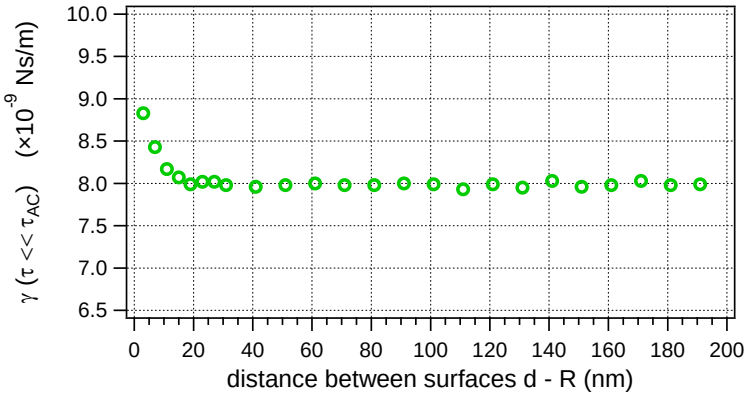

FIGURE S6 BD simulation: Distance-dependent viscous drag $\gamma_\perp(d)$ of a $2R$ = 1 µm bead's diffusive motion perpendicular to a rigid surface, calculated from the slope of the autocorrelation on time scales $\tau \leq 30$ µs. $\gamma_\perp(d)$ is increased to about $1.1 \times \gamma_\infty = 8.8 \times 10^{-9}$ Ns/m for d-R < 9 nm.

The AC(0) = $\langle b_y(t)^2 \rangle$ value, which affects the slope kT/γ used for the calculation of the viscous drag (see Eq. 4 in the main text), experiences qualitatively the same slight distortion for distances d-R < 9 nm, see Fig. S5. This immediately leads to a slight miscalculation of $\gamma_\perp(d)$, also only apparent for d-R < 9 nm, as shown in Fig. S6. As explained above, this systematic, but very small error does not impact the data presented in this study. The effects discussed here are only present in the fluctuation data perpendicular to the interface, i.e., y direction, the parallel directions however remain completely undisturbed (not shown).

In conclusion, we see that a systematic overestimation of $\gamma_\perp(d)$ of maximum 10 % occurs only at distances as small as the bead's fluctuation width, i.e., below 9 nm given the experimental parameters in this study. This is smaller than the chosen step size in our experiments and thus does not affect any data points presented in this paper.

Distance-dependent histogram width

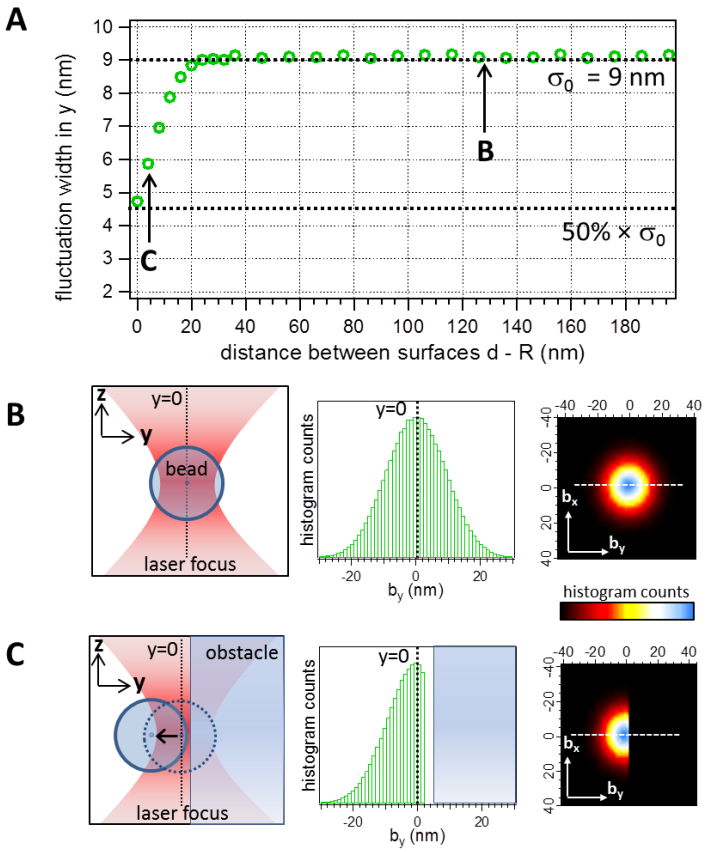

FIGURE S7 BD Simulation: (A) Distance-dependent fluctuation width $\sigma_y(d) = \sigma_\perp(d)$ of a $2R = 1$ µm bead's diffusive motion perpendicular to a rigid surface, calculated as the standard deviation of the fluctuation data. The histogram width $\sigma_\perp(d)$ decreases to 50% of its bulk value at $d = R$. (B) From left to right: Schematic illustration of the bead trapped by an undisturbed laser focus, histogram in y (perpendicular) direction along the white dotted line in the two-dimensional histogram (x-y-plane). (C) Illustration, one-dimensional and two-dimensional histograms for the case of an interface obstructing the bead's diffusive movement inside the optical trap.

Figure S7 *A* shows the distance-dependence of the histogram width perpendicular to an interface. An interface is successively brought closer to an optically trapped bead. As soon as the surface's distance to the trap center is smaller than one bead radius plus its fluctuation width, i.e., $d - R < \sigma_\perp$, the diffusive motion of the bead inside the optical trap is obstructed by the presence of the interface, as seen in Fig. S7 *C*. This results on the one hand in a shift of the bead's mean position $\langle b_y(t) \rangle$, which has been shown and discussed in the context of Fig. S4, and on the other hand in a decreasing fluctuation width σ_y as seen in Fig. S7 *C*, compared to the undisturbed case illustrated in Fig. S7 *B*. The simulation data show that the decrease at $d = R$, i.e., when the bead's surface and the obstacle's surface coincide, is $\sigma_y(d=R) = 50\% \times \sigma_0$, with σ_0 being the undisturbed histogram width in the absence of interfaces. This criterion has been used throughout this study to determine contact point of the bead and the cell membrane**.**

Results of alternative contact point analysis

As discussed in the main text, the membrane contact point cannot be precisely specified due to the optical influence of the pericellular matrix (PCM) on the fluctuation data. Two criteria to determine the contact point have been established and discussed, hereafter referred to as $\sigma_0/2$ and σ_{min} criterion, respectively. The alternative contact point obtained by the σ_{min} criterion is located in average (0.22 ± 0.09) µm behind the $\sigma_0/2$ contact point. The following Tables S1-S3 display the results of the fluctuation analysis, first by application of the $\sigma_0/2$ criterion (black numbers), then by application of the σ_{min} criterion (bold red numbers), for all cell types that were investigated.

TABLE S1 Comparison of hydrodynamic decay lengths Λ_j (mean values ± standard deviation) for various cell types depending on the choice of the membrane contact point criterion.

	J774	**MDCK**	**HT29**	
$\Lambda_\perp$	0.49 ± 0.03	0.65 ± 0.07	0.45 ± 0.03	(value at $\sigma_0/2$)
	0.43 ± 0.08 (-12%)	**0.57 ± 0.13** (-12%)	**0.40 ± 0.08** (-11%)	(value at σ_{min})
$\Lambda_{\parallel}$	0.27 ± 0.02	0.34 ± 0.02	0.28 ± 0.01	(value at $\sigma_0/2$)
	0.24 ± 0.06 (-11%)	**0.31 ± 0.05** (-9%)	**0.28 ± 0.05** (±0%)	(value at σ_{min})

TABLE S2 Comparison of maximum friction coefficient γ_{0j} (mean values ± standard deviation) for various cell types depending on the choice of the membrane contact point criterion.

	J774	**MDCK**	**HT29**	
$\gamma_{0\perp}$	5.11 ± 0.32	5.64 ± 0.28	6.23 ± 0.41	(value at $\sigma_0/2$)
	11.82 ± 0.84 (+131%)	**9.16 ± 0.55** (+62%)	**12.03 ± 0.94** (+93%)	(value at σ_{min})
$\gamma_{0\parallel}$	2.81 ± 0.59	2.83 ± 0.14	2.80 ± 0.27	(value at $\sigma_0/2$)
	3.92 ± 0.17 (+40%)	**4.62 ± 0.18** (+63%)	**4.47 ± 0.28** (+60%)	(value at σ_{min})

TABLE S3 Comparison of mean first passage times t_j for various cell types depending on the choice of the membrane contact point criterion.

	J774	**MDCK**	**HT29**	
$t_\perp$	0.340s (= 1.453×t_0)	0.384s (= 1.642×t_0)	0.326s (= 1.392×t_0)	(value at $\sigma_0/2$)
	0.745s (+119%) **(= 3.182×t_0)**	**0.827s** (+115%) **(= 3.354×t_0)**	**0.694s** (+113%) **(= 2.965×t_0)**	(value at σ_{min})
$t_{\parallel}$	0.259s (= 1.107×t_0)	0.277s (= 1.182×t_0)	0.262s (= 1.119×t_0)	(value at $\sigma_0/2$)
	0.281s (+8%) **(= 1.205×t_0)**	**0.341s** (+23%) **(= 1.457×t_0)**	**0.316s** (+21%) **(= 1.349×t_0)**	(value at σ_{min})

A graphical comparison of the results of Tables S1 – S3 is displayed in Figs. S8 – S10. It becomes obvious that the measurement of the hydrodynamic decay lengths are hardly influenced by the choice of the exact membrane contact point, see Fig. S8. A slight overall decrease of Λ_j in the range of 10% can be seen for all cell types. The maximum viscous drags $\gamma_{0\perp}$ and $\gamma_{0\parallel}$ exhibit a distinct increase of $\gamma_{0\perp}$ and $\gamma_{0\parallel}$, most pronounced in perpendicular direction, see Fig. S9. The change in γ_{0j} und Λ_j also affects the diffusion times t_j, which are significantly enlarged when the membrane is located further away from the 50% σ_0 point, see Fig. S10.

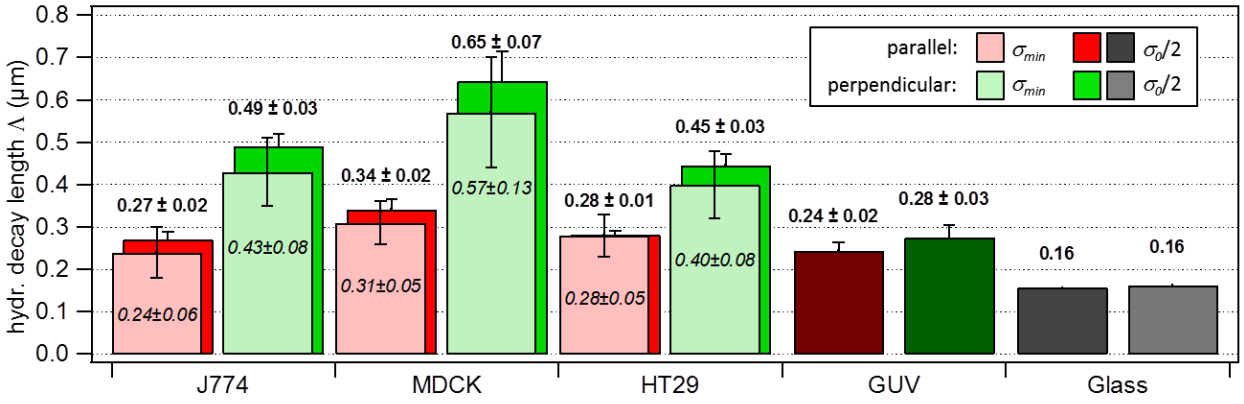

FIGURE S8 Hydrodynamic decay lengths $\Lambda_\perp$ and $\Lambda_\parallel$ for all cell types. The results obtained by the σ_{min} criterion are displayed in light red and green bars (mean values ± standard deviation in italics), bold numbers ± standard deviation and rich red/green bars correspond to membrane location estimated by $\sigma_0/2$.

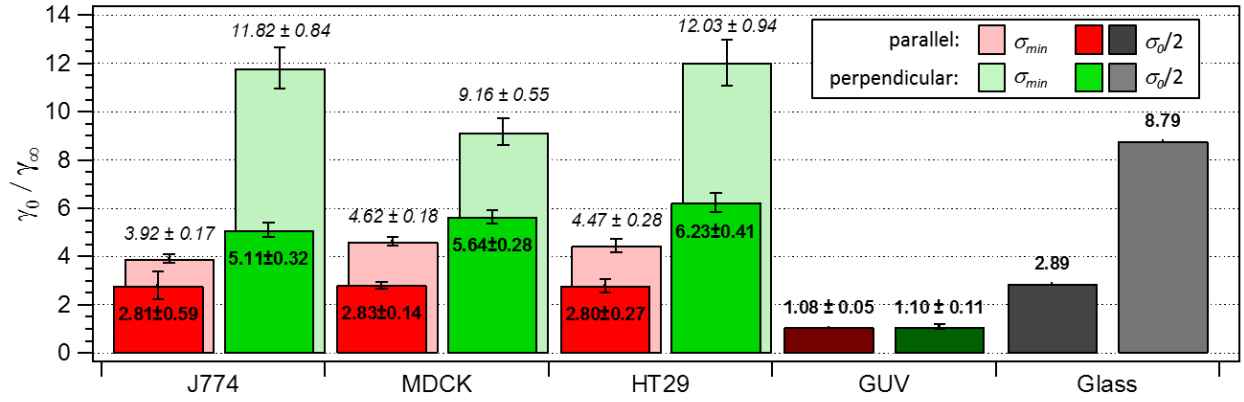

FIGURE S9 Maximum friction coefficient $\gamma_{0\perp}$ and $\gamma_{0|}$ for all cell types. The results obtained by the σ_{min} criterion are displayed in light red and green bars (mean values ± standard deviation in italics), bold numbers ± standard deviation and rich red/green bars correspond to membrane location estimated by $\sigma_0/2$.

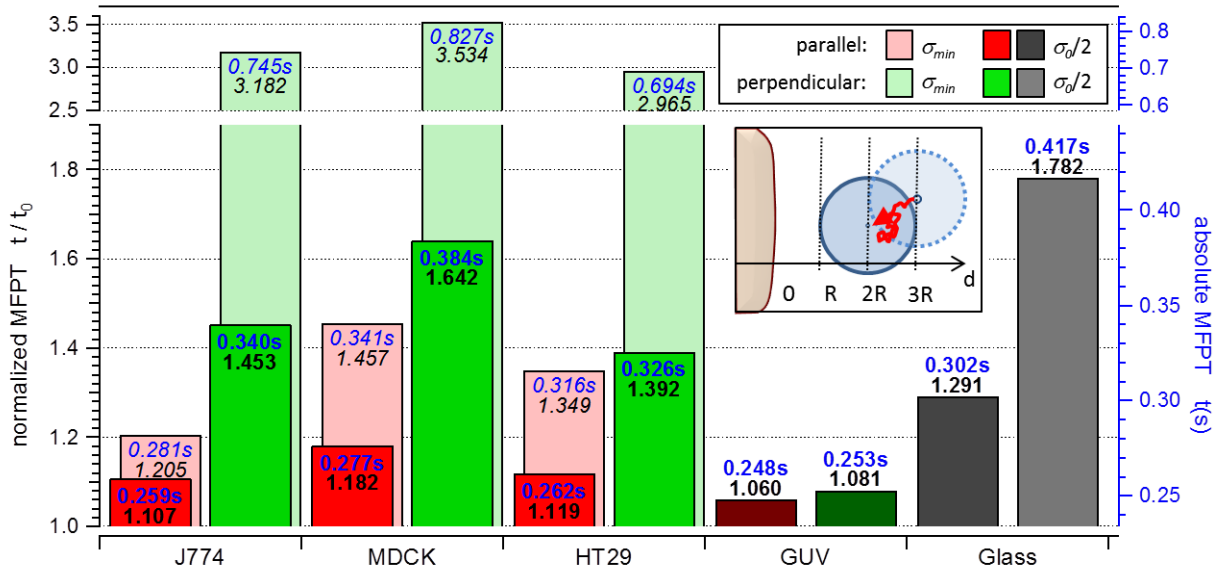

Figure S10 Mean first passage times $t_{0\perp}$ and $t_{0\parallel}$ for all cell types, considering the diffusion of a $2R$ = 1 µm sized bead from $d_1 = 3R$ toward $d_2 = 2R$. The results obtained by the σ_{min} criterion are displayed in light red and green bars (labels in italics), bold labels and rich red/green bars correspond to membrane location estimated by $\sigma_0/2$. Note the axis break between $1.9\times t_0$ and $2.5\times t_0$.

Data recording and fluctuation analysis of a bead approaching a glass interface

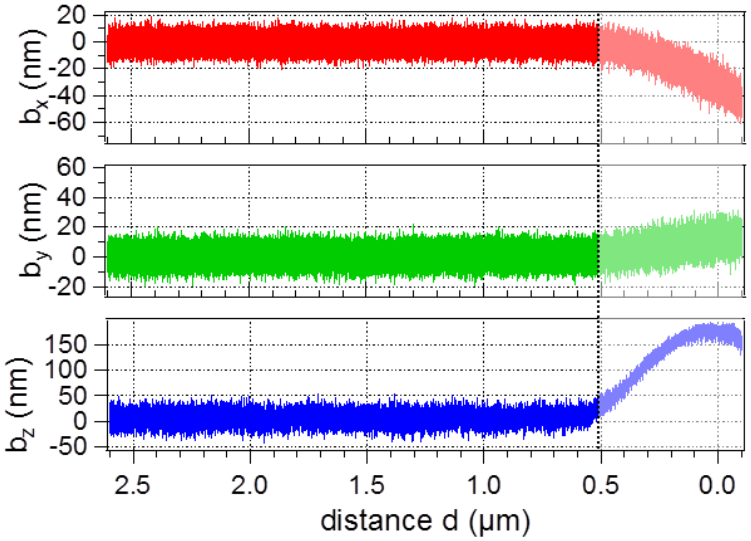

FIGURE S11 Fluctuation data of a 1 µm bead approaching a stiff glass coverslip in *z* direction. Distance-dependent position trajectories $b_x(d,t)$, $b_y(d,t)$, $b_z(d,t)$ calculated from the QPD data after calibration. *z* data correspond to scan direction. Contact between bead and coverslip at $d = R$ is indicated by the black dotted line and the shaded region at $d \leq R$.

The experiments with glass coverslips as obstructing interfaces were performed under slightly different geometrical and experimental conditions. In contrast to the cell experiments, where the surface was approached in lateral (*y*) direction, the glass coverslip was approached in -*z* direction, i.e., in reverse propagation direction of the laser light. The scan was performed over a *z* range of 5 µm, of which roughly 2.5 µm are shown in Fig. S11, with Δz = 20 nm steps as in the cell experiments. To account for the intrinsically weaker trap stiffness in *z* direction compared to *x* and *y*, the laser power was increased to 60 mW compared to 40 mW in cell experiments. This results in increased overall trap stiffnesses compared to the cell experiments, as seen in Fig. S12. Figure S11 displays the distance-dependent fluctuation data calculated from QPD signals via calibration upon approaching the glass coverslip with an optically trapped 1 µm bead. Blue data points (*z* data) correspond to scan direction. The mean signal shift, noticeable already at distances of roughly 1 µm before contact in all cell experiments, is not observed in this experiment due to the different geometrical circumstances: Whereas the cell is placed only at one side of the optical trap, thus asymmetrically scattering the laser light and leading to a shift of the mean signal due to destructive interferences, the glass coverslip is practically infinitely extending to both sides of the laser focus, thus having no optical effect on the QPD signals. The narrowing of the fluctuation data in scan direction becomes apparent as d approaches $d = R$ (contact between bead and coverslip).

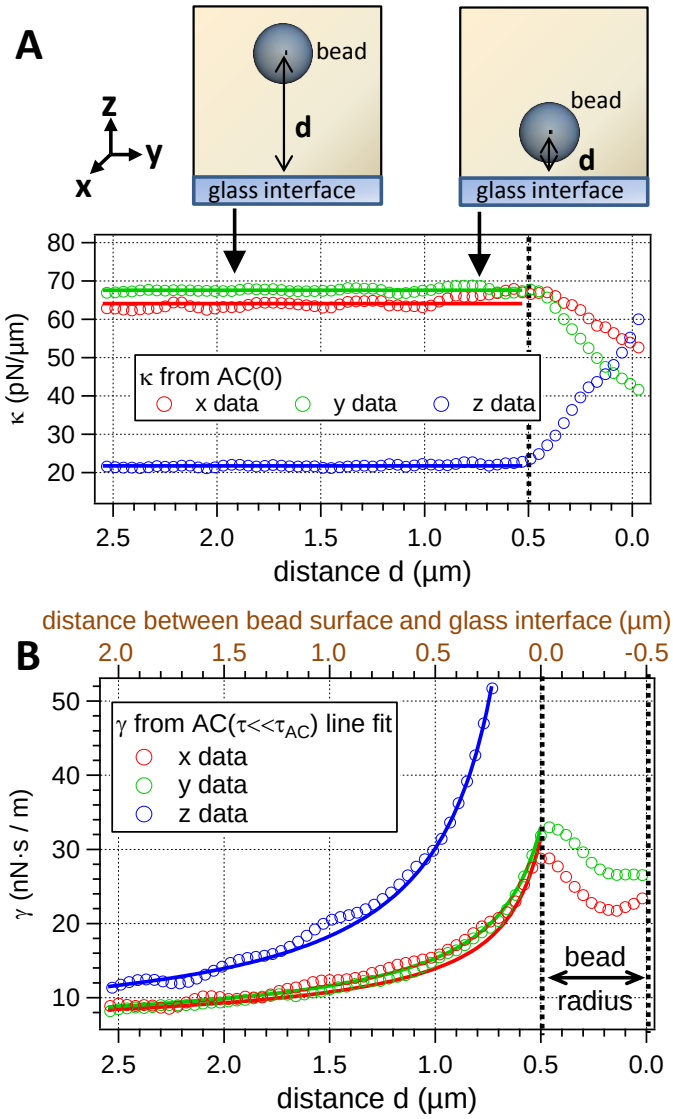

FIGURE S12 The bead's distance d to the glass coverslip is subsequently decreased in z direction (blue data), as illustrated in the schematic sketch. Contact between the bead surface and coverslip is marked by a vertical dotted black line at d = 0.5 µm. (A) The stiffness parameter $\kappa_j(d)$ and (B) the viscous drag $\gamma_j(d)$ are plotted as a function of d. Solid lines indicate fits to the data points according to Happel's & Brenner's formula.

Figure S12 shows that all components κ_j (j = x,y,z) of the stiffness parameter remain constant until mechanical contact between the bead and the coverslip is established, as indicated by additional line fits. The friction coefficients $\gamma_j(d)$ increase as the bead approaches the interface. The increase of the friction component perpendicular to the glass coverslip, i.e., $\gamma_z(d)$ displayed in blue, is significantly higher than $\gamma_x(d)$ and $\gamma_y(d)$ in parallel direction (red and green circles). Happel's and Brenner's formula allows to quantify the distance-dependent behavior of $\gamma_j(d)$ close to a stiff, infinitely large flat interface and was fitted to the data points. Measurement and fit results are in excellent agreement.

Data recording and fluctuation analysis of a bead approaching a GUV

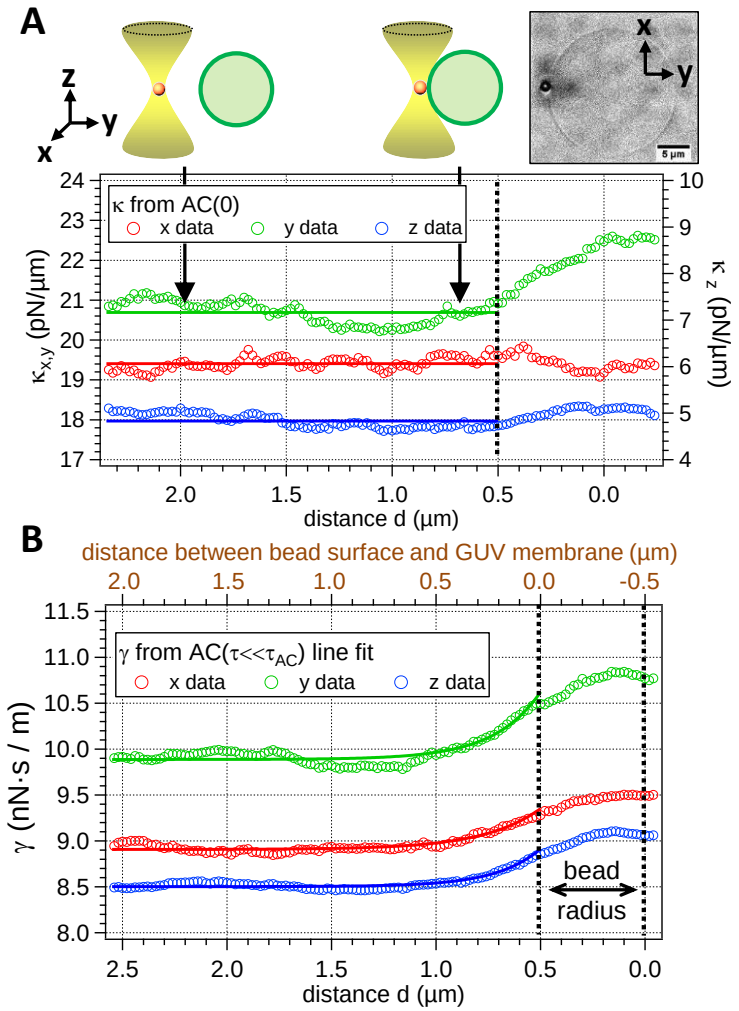

FIGURE S13 Distance-dependent stiffness and viscous drag of a 1 µm bead approaching a GUV. The bead's distance d to the GUV membrane is subsequently reduced in y direction (green data), as illustrated in the schematic sketch. Contact between the bead surface and membrane is marked by a vertical dotted black line at d = 0.5 µm. (A) The stiffness parameter $\kappa_j(d)$ and (B) the viscous drag $\gamma_j(d)$ are plotted as a function of d. Solid lines indicate fits to the data points.

The distance-dependent stiffness and viscous drag upon approaching a GUV membrane are displayed in Fig. S13. Again, a constant $\kappa_j(d)$ can be seen at $d \geq R$, while at the same time $\gamma_j(d)$ increases exponentially. The overall increase in $\gamma_j(d)$ is much smaller than in the cell experiments, regardless of the spatial dimension $j = x,y,z$ and no anisotropic behavior of the hydrodynamic decay length is observed. These results are discussed in detail in the main text. Due to the weaker laser power in the GUV experiment, the overall stiffnesses $\kappa_j(d)$ are smaller than in the cell experiments. However, as the viscous drag $\gamma_j(d)$ is independent of the choice of experimental parameters like laser power, results for $\gamma_j(d)$ are comparable with those obtained from cell experiments.

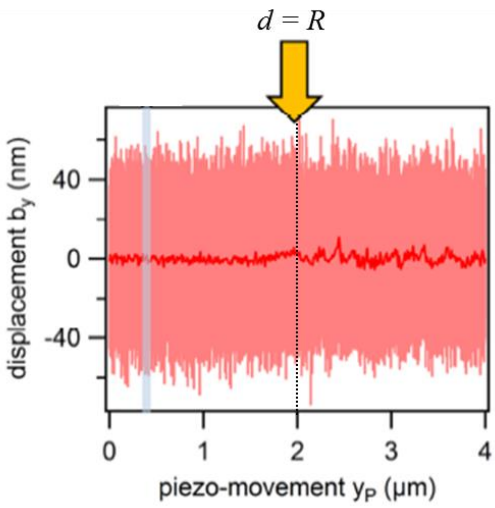

FIGURE S14 Bead displacement $b_y(d)$ upon approaching a GUV membrane. Light red data show the bead's trajectory in scan direction while the piezo stage (coordinate y_p) was successively moved towards the GUV membrane. The dark red curve shows the smoothed trajectory. Contact between bead surface and membrane of the unfixed GUV at $d=R$, corresponding to y_p = 2 µm in this experiment, is indicated by the dotted black line and the yellow arrow. Illustration was taken from (3) with the author's permission.

Figure S14 shows the calibrated bead's trajectory in scan direction upon approaching the membrane of an unfixed GUV. After contact, the 20 µm large GUV is dragged to the side by the moving bead. The method to determine the contact point $d = R$ is described in (3) and shall not be explained here.

Frequency-dependence of the viscous drag

In general, the viscosity in direction $j = \perp,\parallel$ is frequency-dependent. Fourier transformation of the overdamped Langevin (Eq. 1 in the main text) yields:

$$\tilde{b}_j(\omega)\cdot\left(i\omega\cdot\tilde{\gamma}_j(\omega,d)+\kappa_{opt,j}-\tilde{\kappa}_{cell,j}(\omega,d)\right)=\tilde{F}_{th,j}(\omega) \tag{S3}$$

As long as no binding to the membrane or to cellular protrusions occurs, the system consisting of bead and surrounding fluid is in thermal equilibrium. Thus, the fluctuation-dissipation-theorem and the Kramers-Kronig relations can be applied to extract the storage and loss moduli $G'(\omega)$ and $G''(\omega)$ from the fluctuation data (2). In this case, the loss modulus $G''(\omega)=1/6\pi R\cdot\omega\cdot\tilde{\gamma}(\omega)$ increases with the frequency-dependent drag coefficient $\tilde{\gamma}(\omega)$, but amplifies higher frequencies by the multiplication with ω. Details of the calculation procedure can be found in (4, 5).

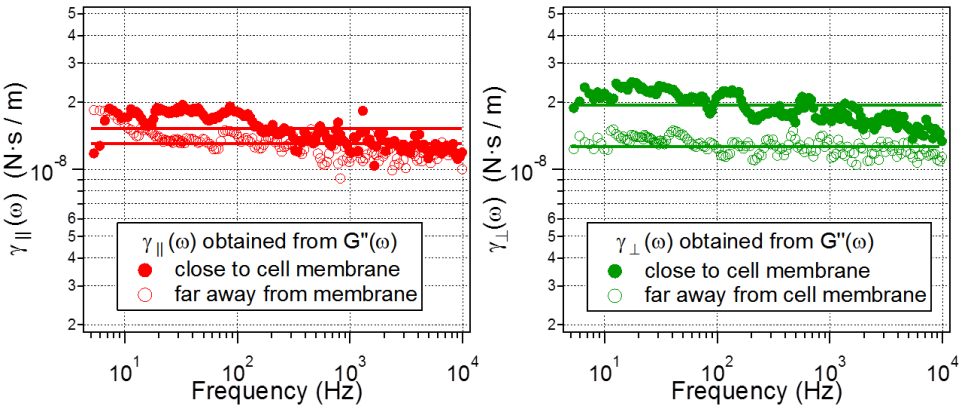

FIGURE S15 Frequency-resolved viscous drag $\gamma_j(\omega)$ ($j = \perp,\parallel$) for two different distances to the membrane of a MDCK cell. Hollow circles denote data recorded far away from the membrane (d-$R >> \Lambda$), full circles represent a distance of approximately d-R = 0.3 µm. The solid lines indicate fits to the data points.

Figure S15 displays the frequency-dependent viscous drag $\tilde{\gamma}(\omega)$ for two different distances d between bead and cell. Here, hollow circles represent a distance $d-R \gg \Lambda_{\parallel,\perp}$ much larger than the measured hydrodynamic decay length and solid circles represent a small distance $d-R=0.3\,\mu\text{m}<\Lambda_{\parallel,\perp}$. Red and green colors denote parallel and perpendicular particle motions, respectively. It is apparent from Fig. S15 that $\tilde{\gamma}(\omega)$ remains approximately constant over the whole frequency range under investigation ($\omega/2\pi \leq 10$ kHz), both for parallel and perpendicular data. Nearby the cell membrane, the mean value $\gamma_\parallel(\omega)$ increases only modestly by 18%, whereas the mean $\gamma_\perp(\omega)$ increases by 51%. Again, it can be seen that the rise of the mean value of $\gamma_\perp$ for short particle-cell distances is higher than the rise of the mean $\gamma_\parallel$. The slow drop-off at high frequencies is ascribed to numerical artifacts during calculation, resulting from a finite upper frequency limit (6). Also, reliable results are only obtained up to a maximum frequency of about 10 kHz due to the finite maximum frequency. The results exemplarily presented in this chapter agree with $\gamma_\perp$ and $\gamma_\parallel$ obtained from the procedure described in Eq. 2 and presented in Fig. 6 in the main text. Furthermore, it can be seen that $\gamma_j(d)$ has no frequency-dependent contribution and that averaging over all frequencies ω is justified.

Visco-elastic analysis of the fluctuation data via passive microrheology

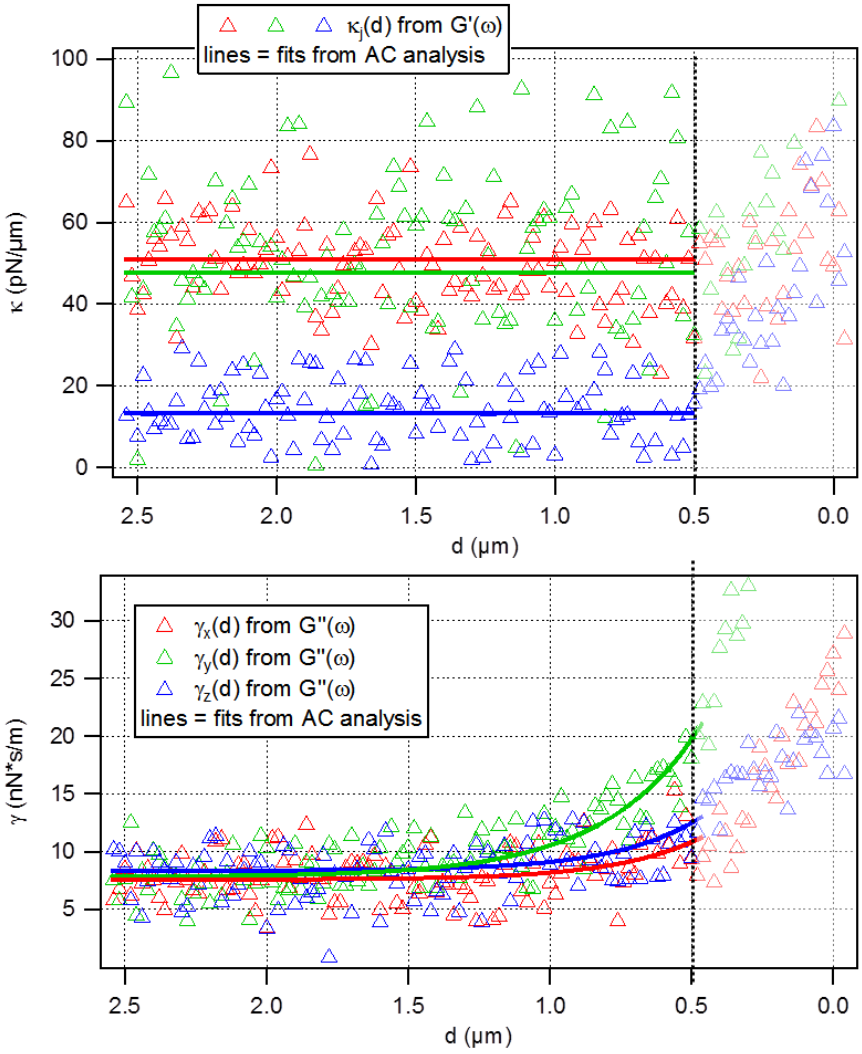

FIGURE S16 Analysis of the fluctuation data of a 1 µm bead approaching a HT29 cell membrane via passive microrheology. (A) The distance-dependent stiffness parameter $\kappa_j(d)$ was calculated from the real part of the complex shear modulus, $G'(\omega) = Re(G(\omega))$. (B) The imaginary part $Im(G(\omega)) = G''(\omega)$ was used to calculate the viscous drag $\gamma_j(d)$.

The fluctuation data that was shown in Fig. 4 in the main text was analyzed with the help of the microrheology toolbox, that has been shortly introduced in the previous paragraph and, e.g., in (4, 5).

In brief, the linearized response function $\alpha(\omega)$ of a spherical particle with radius R displaced by $\tilde{b}(\omega)$ reacts to a driving force such that $\tilde{b}(\omega) = \alpha(\omega) \cdot \tilde{F}(\omega)$. $\alpha(\omega)$ is inversely proportional to

the complex shear modulus $G(\omega) = (6\pi R \cdot \alpha(\omega))^{-1}$. For a thermal driving force $\tilde{F}_{th,j}(\omega)$ it follows from Eq. S3 that

$$\alpha_j(\omega) = \frac{\tilde{b}_j(\omega)}{\tilde{F}_{th,j}(\omega)} = \frac{1}{i\omega \cdot \tilde{\gamma}_j(\omega,d) + \kappa_{opt,j} - \tilde{\kappa}_{cell,j}(\omega,d)} \ , \tag{S4}$$

resulting in the complex shear modulus

$$G_j(\omega) = \frac{\kappa_{opt,j} - \tilde{\kappa}_{cell,j}(\omega,d) + i\omega \cdot \tilde{\gamma}_j(\omega,d)}{6\pi R} \tag{S5}$$

with real and imaginary parts

$$G_j'(\omega) = \frac{\kappa_{opt,j} - \tilde{\kappa}_{cell,j}(\omega,d)}{6\pi R} \qquad \text{and} \qquad G_j''(\omega) = \frac{\tilde{\gamma}_j(\omega,d) \cdot \omega}{6\pi R} . \tag{S6}$$

Eq. S6 shows that the real part (accounting for elastic components) and the imaginary part (viscous component) of the complex shear modulus are independent of each other. Therefore, the increase in $\kappa_y(d)$ on the last 0,2 µm before contact, as seen in Fig. 4, does not lead to a miscalculation of $\gamma(d)$. This increase is probably due to transient binding to the glycocalyx surrounding the cell membrane.

Figure S16 shows the stiffness $\kappa_j(d)$ and viscous drag $\gamma_j(d)$ of the very same data presented in Fig. 4, calculated by Eqs. S4-S6. The resulting noise is inherent to passive microrheological data analysis via Kramers-Kronig transform. Nevertheless, the rather constant behavior of $\kappa_j(d)$ ($j=x,y,z$) can be observed, as indicated by the line fits from Fig. 4. Also, the smooth increase in $\gamma_j(d)$ can still be seen in Fig. S16, visualized by least-square fits which reveal the same result as those plotted in Fig. 4.

In conclusion, we have shown that the transient binding, be it to the glycocalyx or to any other structure surrounding the cell membrane, does not corrupt the correct measurement of $\gamma_j(d)$. Figure S16 confirms the theoretical concept presented above despite the relatively strong scattering of the data points.

SUPPORTING REFERENCES

1. Grassia, P. S., E. J. Hinch, and L. C. Nitsche. 1995. Computer Simulations of Brownian Motion of Complex Systems. J. Fluid Mech. 282:373-403.
2. Landau, L. D., and E. M. Lifshitz. 1969. Statistical Physics. Pergamon Press, Oxford, UK.
3. Meinel, A., B. Tränkle, W. Römer, and A. Rohrbach. 2014. Induced phagocytic particle uptake into a giant unilamellar vesicle. Soft Matter 10 3667 - 3678.
4. Buchanan, M., M. Atakhorrami, J. F. Palierne, F. C. MacKintosh, and C. F. Schmidt. 2005. High-frequency microrheology of wormlike micelles. Phys. Rev. E 72:011504.
5. Gittes, F., B. Schnurr, P. D. Olmsted, F. C. MacKintosh, and C. F. Schmidt. 1997. Microscopic viscoelasticity: Shear moduli of soft materials determined from thermal fluctuations. Phys. Rev. Lett. 79:3286-3289.
6. Schnurr, B., F. Gittes, F. C. MacKintosh, and C. F. Schmidt. 1997. Determining microscopic viscoelasticity in flexible and semiflexible polymer networks from thermal fluctuations. Macromolecules 30:7781-7792.